Monthly Notices
of the
ROYAL ASTRONOMICAL SOCIETY

Mon. Not. R. Astron. Soc. **408,** 1335–1360 (2010) doi:10.1111/j.1365-2966.2010.17091.x

SPIDER – II. The Fundamental Plane of early-type galaxies in *grizYJHK*

F. La Barbera,[1⋆] R. R. de Carvalho,[2⋆] I. G. de la Rosa[3,4] and P. A. A. Lopes[5]

[1] *INAF – Osservatorio Astronomico di Capodimonte, Salita Moiariello 16, 80131 Napoli, Italy*
[2] *Instituto Nacional de Pesquisas Espaciais, Avenida dos Astronautas, 1758 S. J. dos Campos, SP 12227-010, Brazil*
[3] *Instituto de Astrofísica de Canarias (IAC), E-38200 La Laguna, Tenerife, Spain*
[4] *Depto de Astrofísica, Universidad de La Laguna (ULL), E-38206 La Laguna, Tenerife, Spain*
[5] *Observatório do Valongo, Universidade Federal do Rio de Janeiro, Ladeira do Pedro Antônio 43, Rio de Janeiro, RJ 20080-090, Brazil*

Accepted 2010 May 26. Received 2010 May 25; in original form 2009 December 23

ABSTRACT

We present a complete analysis of the Fundamental Plane (FP) of early-type galaxies (ETGs) in the nearby Universe ($z < 0.1$). The sample, as defined in Paper I, comprises 39 993 ETGs located in environments covering the entire domain in local density (from field to cluster). We derive the FP in the *grizYJHK* wavebands with a detailed discussion on fitting procedure, bias due to selection effects and bias due to correlated errors on the effective parameters, r_e and $\langle\mu\rangle_e$, as key factors in obtaining meaningful FP coefficients. Studying the Kormendy relation (KR) we find that its slope varies from g (3.44 ± 0.04) through K (3.80 ± 0.02) implying that smaller size ETGs have a larger ratio of optical to near-infrared (NIR) radii than galaxies with larger r_e. We also examine the Faber–Jackson (FJ) relation and find that its slope is similar for all wavebands, within the uncertainties, with a mean value of 0.198 ± 0.007. Writing the FP equation as $\log r_e = a \log \sigma_0 + b\langle\mu\rangle_e + c$, we find that the '$a$' varies from 1.38 ± 0.02 in g to 1.55 ± 0.02 in K, implying a 12 per cent variation across the *grizYJHK* wavelength baseline. The corresponding variation of 'b' is negligible ($b \sim 0.316$), while 'c' varies by $\sim$10 per cent. We show that the waveband dependence of the FJ and KR results from the complex variation of the distribution of galaxies in the face-on projection of the FP as well as by the change of FP coefficients with waveband. We find that 'a' and 'b' become smaller for higher Sersic index and larger axial ratios, independent of the waveband. This suggests that these variations are likely to be related to differences in structural and dynamical (rather than stellar population) properties of ETGs. It is noticeable that galaxies with bluer colours and disc-like isophotes have smaller 'b', with the effect decreasing smoothly from g through K. Considering a power-law relation between mass-to-light ratio and (dynamical) mass, $M/L \propto M^{\gamma}$, we estimate γ from the FP coefficients in *grizYJHK*. The γ decreases from 0.224 ± 0.008 in g to 0.186 ± 0.009 in K band. Using the γ values, we estimate the variation of age and metallicity of the stellar populations present in massive galaxies per decade in stellar mass. This analysis shows that in the NIR the tilt of the FP is not due to stellar population variation, and that ETGs have coeval stellar populations with an age variation of a few per cent per decade in mass, and a corresponding metallicity increase of $\sim$23 per cent. We also show that current semi-analytical models of galaxy formation reproduce very well these amounts of variation of age and metallicity with respect to stellar mass.

Key words: galaxies: evolution – galaxies: formation – galaxies: fundamental parameters.

1 INTRODUCTION

One of the most outstanding and basic cosmological questions is how galaxies form and evolve. Currently the favoured scenario assumes that the assemblage of baryonic matter is driven by the evolution of dark matter haloes (Gott & Rees 1975). Given the difficulty of observing dark matter, we rely on the luminous counterpart to be a beacon illuminating their evolution. The vast majority of stars and metals produced during the evolution of galaxies were formed and still reside in them. Therefore, examining the star formation history and measuring the metal content of galaxies may tell us how these systems evolve through cosmic time.

⋆E-mail: labarber@na.astro.it (FLB); rrdecarvalho2008@gmail.com (RRdC)

The study of the global properties of elliptical galaxies took a substantial step forward with the application of multivariate analysis, revealing potentially meaningful scaling relations like the Fundamental Plane (FP; Brosche 1973). However, the importance of the technique pioneered by this paper was not immediately realized by the astronomical community. Determining which dimensions are statistically significant in a given data set is not a simple task, but it can reveal useful correlations involving the quantities defining a minimal manifold and provide insights into the physical nature of such correlations. Such is the case when the observed FP is associated with the virial theorem (Djorgovski & Davis 1987; Dressler et al. 1987).

Many studies over the past twenty years have tried to interpret the physical meaning of the FP (e.g. Faber et al. 1987; Djorgovski & de Carvalho 1990; Jørgensen, Franx & Kjærgaard 1996, hereafter JFK96; Pahre, de Carvalho & Djorgovski 1998a; Jørgensen et al. 1999; Bernardi et al. 2003a,b,c; Dantas et al. 2003; Nelan et al. 2005; Cappellari et al. 2006). The striking feature of the FP is its narrowness, implying a regularity among the global properties of early-type galaxies (ETGs). The quantities containing the entire variance of the data are effective radius, $r_{\rm e}$, central velocity dispersion, $\sigma_{\circ}$, and mean surface brightness measured within the effective radius, $\mu_{\rm e}$. The best representation of the FP is $r_{\rm e} \sim \sigma_{\circ}^{A} I_{\rm e}^{B}$, where $I_{\rm e}$ is mean surface brightness in flux units. Bernardi et al. (2003c) show a comprehensive table listing the most important papers presenting values of A and B and their respective errors. A seems to vary with the passband used in the photometric observation, while B does not (see e.g. Pahre et al. 1998a; Scodeggio et al. 1998; Mobasher et al. 1999). However, Bernardi et al. (2003c) found only a marginally significant variation of A in the SDSS optical passbands (see also Hyde & Bernardi 2009). La Barbera et al. (2008b, hereafter LBM08) also found a small difference in A when measured between r and K bands.

Assuming that ETGs are homologous systems in dynamical equilibrium and that velocity dispersion is related to the kinetic energy per unit mass we can write down expressions for mass (M) and luminosity (L), namely $(M/L) \sim \sigma^{2-A} I^{-1-B}$. In the case of a fully virialized system, $A = 2$ and $B = -1$, implying a constant mass-to-light ratio. However, A and B are found to differ significantly from the virial values, resulting in the so-called tilt of the FP. In this case, $M/L \sim M^{\gamma}$, where γ is $\sim$0.25 (Faber et al. 1987). This dependence of the mass-to-light ratio on galaxy mass has been interpreted as arising either from differences in the stellar populations or the dark matter fractions among ETGs. It is important to emphasize that another option to explain the tilt is related to the assumption that ETGs are truly virialized systems – in which case they should have self-similar density distributions and similar orbital distributions. Any departure from either or both of these conditions may well explain the tilt, and several studies have tried to disentangle these effects. For instance, non-homology seems to contribute to at least part of the tilt (Capelato, de Carvalho & Carlberg 1995; Hjorth & Madsen 1995; Ciotti, Lanzoni & Renzini 1996; Busarello et al. 1997; Ciotti & Lanzoni 1997; Graham & Colless 1997; Bertin, Ciotti & del Principe 2002; Trujillo, Burkert & Bell 2004). Even studies trying to explain the tilt as a stellar population effect concluded that non-homology may play a significant role in determining the tilt of the FP (e.g. Pahre et al. 1998a; Forbes & Ponman 1999). Another interesting finding from the simulations of Capelato et al. (1995) is that when measuring the structural parameters defining the FP inside larger apertures, of order a few $r_{\rm e}$, the coefficients are similar to those implied by the virial theorem. More recently, Bolton et al. (2008) find a similar result when using the surface density term defined by the mass measured through strong lensing, and conclude that the tilt of the FP is due to the fraction of dark matter inside one effective radius (see also Tortora et al. 2009).

This is the second paper of a series analysing the properties and the scaling relations of ETGs as a function of the environment where they reside. The Spheroids Panchromatic Investigation in Different Environmental Regions (SPIDER) utilizes optical and near-infrared (NIR) photometry in the *grizYJHK* wavebands, along with spectroscopic data, taken from the UKIRT Infrared Deep Sky Survey-Large Area Survey (UKIDSS-LAS) and the Sloan Digital Sky Survey (SDSS). The selection of ETGs for this project is detailed in Paper I, and we refer the reader to that paper for all the details of sample selection and the procedures used to derive the galaxy parameters.

In this work we focus on the derivation of the FP in the *grizYJHK* wavebands for the entire SPIDER sample. Although our sample contains ETGs over the entire domain of local density (from field to clusters), we postpone the study of the environmental dependence of the FP to another paper in the SPIDER series (Paper III). In the present work, we discuss the main pitfalls of the FP fitting procedure and how to account for selection effects and different sources of biases. We analyse the edge-on and face-on projections of the FP, as well as the two other projections of the FP, i.e. the Kormendy relation (KR) and Faber–Jackson (FJ) relation. The analysis of these two scaling relations serves as a reference at the local Universe ($z < 0.1$), and at different wavebands, for other studies lacking data for a full FP analysis. We find a consistent picture connecting the waveband variation of the edge- and face-on projections of the FP with that of the KR and FJ relation. Finally, we show how the optical and NIR FPs can constrain various scenarios for galaxy formation and evolution, by using the wavelength dependence of the FP to infer the variation of stellar population parameters along the ETG's sequence.

The layout of the paper is as follows. Section 2 shortly describes the SPIDER data set. Section 3 presents the different subsamples of ETGs used to derive the FP in *grizYJHK* and to analyse the impact of different biases on the FP. Section 4 details the FP fitting procedure. Sections 5 and 6 analyse the KR and FJ relation, respectively. Section 7 presents one main result of this study, i.e. the dependence of FP slopes on waveband, from g through K. Section 8 analyses the waveband variation of the edge- and face-on projections of the FP. Section 9 describes how the optical and NIR scaling relations of ETGs constrain the variation of stellar population properties along the FP. Discussion follows in Section 10. A summary is provided in Section 11.

Throughout the paper, we adopt a cosmology with $H_0 = 75\,{\rm km\,s^{-1}\,Mpc^{-1}}$, $\Omega_{\rm m} = 0.3$ and $\Omega_{\Lambda} = 0.7$.

2 DATA

The SPIDER data set is based on a sample of 39 993 ETGs (see Paper I for details), with available *griz* photometry and spectroscopy from SDSS Data Release 6 (DR6). Out of these galaxies, 5080 objects have also photometry available in the *YJHK* wavebands from UKIDSS-LAS. All galaxies have two estimates of the central velocity dispersion, one from SDSS DR6 and an alternative measurement obtained by fitting SDSS spectra with the software STARLIGHT (Cid Fernandes et al. 2005), using a linear combination of simple stellar population models (rather than single templates as in SDSS) with different ages and metallicities. In both cases, STARLIGHT and SDSS DR6, the σ_0s are aperture corrected to an aperture of $r_{\rm e}/8$, following Jørgensen, Franx & Kjærgaard (1995). In order to make

proper comparisons to earlier studies (e.g. Bernardi et al. 2003a), we use SDSS velocity dispersion measurements to examine the scaling relations presented in this paper. In Paper I, we find that the mean difference between σ_0 (SDSS DR6) and σ_0 (STARLIGHT) does not change significantly with σ_0. Therefore, we do not expect that the choice of a given velocity dispersion measurement might have a dramatic impact on the FP relation. This is further discussed in Sections 6, 7 and 9.

In all wavebands, structural parameters – i.e. the effective radius, r_e, the mean surface brightness within that radius, $\langle\mu\rangle_e$, and the Sersic index, n – have been all homogeneously measured by 2DPHOT (La Barbera et al. 2008a). In the optical (*griz*), alternative estimates of the effective parameters, r_e and $\langle\mu\rangle_e$, are also available from the SDSS DR6 PHOTO pipeline. In Paper I, we compare the different estimates of photometric and spectroscopic parameters, deriving also an estimate of the 95 per cent completeness limit of the sample in all wavebands. We find that 2DPHOT total magnitudes are brighter than SDSS model magnitudes, with the difference amounting to $\sim$0.2 mag in r band, for the faintest galaxies in the sample. This difference is due to the use of Sersic (2DPHOT) rather than de Vaucouleurs (PHOTO) models to fit the light distribution of ETGs, as well as to the sky estimate bias affecting SDSS effective parameters (Adelman-McCarthy et al. 2008; Abazajian et al. 2009). Hence, the completeness limit of the sample is also dependent on the source of effective parameters (2DPHOT versus PHOTO). In r band, the sample is 95 per cent complete at -20.32 and -20.55 for the SDSS and 2DPHOT parameters, respectively. In the following, unless explicitly said, we refer to 2DPHOT total magnitudes.

3 THE SAMPLES

The waveband dependence of the FP is analysed using different subsamples of ETGs, extracted from the SPIDER sample. Details on each subsample are provided in Section 3.1. In order to analyse the effect of different sources of bias on the FP relation, we also utilize several samples of ETGs, with effective parameters in r band. We describe the characteristics of these samples in Section 3.2, referring to them, hereafter, as the control samples of ETGs.

3.1 The *grizYJHK* (SDSS+UKIDSS) samples of ETGs

In order to analyse how different selection procedures might affect the dependence of the FP relation on waveband, we derive the FP in the *grizYJHK* wavebands for ETG's SPIDER subsamples defined by two different selection procedures. In case (i), we derive the FP for the same sample of ETGs in all wavebands, by selecting those galaxies brighter than the r-band completeness limit ($^{0.07}M_r = -20.55$). We exclude galaxies whose Sersic fit, in one of the available wavebands, has a high reduced χ^2 value ($\geq$3). This cut removes less than 2 per cent of galaxies, resulting in a sample of 4589 ETGs. In case (ii), we select different samples of ETGs in the different wavebands, but according to *equivalent* magnitude limits. The equivalent magnitude limits are derived by using the optical–NIR colour–magnitude (CM) relations (see section 4 of Paper I). To this effect, we first fix the r-band magnitude limit to -20.6 and then translate it into the other wavebands using the CM relations. The value of -20.6 is chosen so that, for each band, the equivalent magnitude limit is brighter than the completeness magnitude in that band, as defined in Paper I. This makes the samples magnitude complete in all wavebands. The *equivalent* magnitude limits are reported in column 2 of Table 1, along with the 95 per cent completeness magnitude limits, from Paper I, in column 3, as well as the number of ETGs selected in each band in column 4.

Table 1. Magnitude limits in *grizYJHK* adopted to derive the FP.

Waveband	X^a	$^{0.07}M_X$ limit	N_X
g	-19.75	-19.71	4467
r	-20.60	-20.55	4478
i	-21.02	-20.99	4455
z	-21.34	-21.22	4319
Y	-22.03	-21.95	4404
J	-22.55	-22.54	4317
H	-23.22	-23.21	4376
K	-23.60	-23.60	4350

[a] X is the equivalent magnitude limit as used in the colour-selected samples.

In the following, we refer to the ETG sample of case (i) as the (r band) magnitude-selected sample of ETGs, while the samples of case (ii) are referred to as the colour-selected samples of ETGs.

3.2 Control samples of ETGs

We use five control samples of ETGs selected from SDSS DR6, with photometry available in r band. The control samples consist of ETGs selected in different redshift ranges, with effective parameters and central velocity dispersions measured with different methods. In all cases, velocity dispersions are corrected to an aperture of $r_e/8$, following Jørgensen et al. (1995). Each control sample is named with a letter, as shown in Table 2, where we summarize the basic characteristics of the five samples.

(1) Sample A is obtained from the sample of 39 993 ETGs defined in Paper I. We select all galaxies with an r-band model magnitude brighter than -20.32. This magnitude cut corresponds to the 95 per cent completeness limit in r band, as defined in Paper I, when using SDSS model magnitudes (see Section 2). Effective parameters are obtained from SDSS, as in Bernardi et al. (2003a).

(2) Sample B is a subsample of sample A, consisting of all the ETGs that also have photometry available in the *YJHK* wavebands (see Paper I). Such sample is used to estimate the impact of matching SDSS to UKIDSS data on the FP relation.

(3) Sample C is defined to explore a wider magnitude range than that of samples A and B. We query the SDSS DR6 data base for ETGs in a redshift range of $z = 0.02$ to 0.03. ETGs are defined according to the same criteria as in Paper I, i.e. zwarning $= 0$, eclass < 0 and fracDev$_r > 0.8$. No requirement is done for the galaxy velocity dispersion. The query results into a list of 3732 galaxies, that hereafter we refer to as the low-redshift sample of ETGs. All galaxies have effective parameters from SDSS. Using the same procedure as in Paper I, we estimate a 95 per cent completeness limit of $^{0.07}M_r = -17.64$ (model magnitude). Since velocity dispersions from SDSS are not available for all galaxies in this sample, we assign fake σ_0 values to each pair of r_e and $\langle\mu\rangle_e$ values, as described in Section 4.2.

(4) Samples D and E are defined in the same way as samples A and B, respectively, but using 2DPHOT rather than SDSS effective parameters. For both samples, we select all the ETGs in the SPIDER sample with total magnitude brighter than $^{0.07}M_r = -20.5$x5 (corresponding to the 2DPHOT completeness magnitude). Sample E is obtained from sample D by selecting only those objects with matched photometry in UKIDSS. Sample E coincides with the magnitude-selected sample of ETGs in r band (Section 3.1).

Table 2. Control samples of ETGs.

	A	B	C	D	E
Number of galaxies	37 273	4796	3690	36 205	4589
Redshift range	$0.05 \leq z \leq 0.095$	$0.05 \leq z \leq 0.095$	$0.02 \leq z \leq 0.03$	$0.05 \leq z \leq 0.095$	$0.05 \leq z \leq 0.095$
Limiting $^{0.07}M_r$	-20.32	-20.32	-17.64	-20.55	-20.55
Source of r_e and $\langle\mu\rangle_e$	SDSS	SDSS	SDSS	2DPHOT	2DPHOT
Available wavebands	*r*	*grizYJHK*	*r*	*r*	*grizYJHK*

4 DERIVING THE FP

We write the FP relation as

$$\log r_e = a \log \sigma_0 + b\langle\mu\rangle_e + c, \quad (1)$$

where a and b are the slopes, and c is the offset. We denote the rms of residuals around the FP with respect to $\log r_e$ as s_{r_e}, referring to a, b, c and s_{r_e} as the coefficients of the FP. We estimate the FP coefficients by a procedure consisting of three steps. First, we derive the values of a and b, as described in Section 4.1. The slopes are then corrected for different sources of biases, including selection effects (Section 4.2) and the effect of correlated uncertainties on $\log r_e$ and $\langle\mu\rangle_e$, (Section 4.3). The bias-corrected values of a and b are then used to estimate c and s_{r_e} (Section 4.1). This procedure is tested through the ETG's control samples, as discussed in Section 4.4.

4.1 Fitting procedure

We obtain a first estimate of a and b by minimizing the sum of absolute residuals around the FP. When compared to the ordinary least-squares fitting method, where one minimizes the sum of squared residuals, this procedure is more robust, being less sensitive to outliers in the distribution of data points around the plane (JFK96). We adopt two different fitting methods, by minimizing the residuals in $\log \sigma_0$ and the orthogonal residuals about the plane. The orthogonal fit – adopted in most of previous works – has the main advantages of treating all the variables symmetrically, while the $\log \sigma_0$ regression is essentially independent of selections effects in the plane of effective parameters, such as the magnitude limit (see La Barbera, Busarello & Capaccioli 2000, hereafter LBC00). The values of a and b are corrected for selection effects and correlated errors on effective parameters (see Sections 4.2 and 4.3). The value of c is then derived as the median value of the quantity $\log r_e$–$a \log \sigma_0$–$b\langle\mu\rangle_e$, over all the galaxies of a given sample, with a and b being the bias-corrected values of FP slopes. As shown in Section 4.2, when compared to the more common practise of estimating c through the least-squares procedure itself, the above estimate has the advantage of providing an unbiased value of c, regardless of the magnitude selection of the sample. For both fitting methods, we calculate the scatter of the FP, s_{r_e}, from the mean value of the absolute residuals in $\log r_e$ around the plane, using the bias-corrected slopes. As for c, this procedure provides an unbiased estimate of the FP scatter (see Section 4.2).

4.2 Bias due to selection effects

To estimate how selection criteria (e.g. the magnitude limit) affect the FP coefficients, we use a simulated sample of data points in the space of $\log r_e$, $\langle\mu\rangle_e$ and $\log \sigma_0$, resembling the distribution of ETGs in that space. The simulated sample is created from the control sample C, namely all ETGs from SDSS DR6 in the redshift range of 0.02 to 0.03, brighter than an r-band model magnitude of $^{0.07}M_r = -17.64$ (Section 3.2). Since galaxies in this sample do not have available velocity dispersions, we assign fake σ_0 values. For each galaxy, we use its $\log r_e$ and $\langle\mu\rangle_e$ to obtain a value of σ_0 from the FP relation (equation 1). That value is then shifted according to a random Gaussian deviate, with a given width value s_{σ_0}, that describes the scatter of the FP along the σ_0 axis. The slopes, offset and scatter parameters are chosen with an iterative procedure.

(1) First, we select all galaxies in sample C with available σ_0 from SDSS DR6, applying similar cuts in magnitude and velocity dispersion as those for the r-band magnitude-selected sample of ETGs (sec Section 3.1). This is done by selecting all galaxies with model magnitude brighter than -20.28[1] and $70 \leq \sigma_0 \leq 420\,\mathrm{km\,s^{-1}}$. This subsample consists of 1682 ETGs out of 3690 galaxies in sample C. We derive the best-fitting FP coefficients for this subsample, referring to them as the *reference* coefficients of the FP.

(2) We assign fake σ_0 values to sample C by using guess values of a, b, c and s_{σ_0}. Applying the same cuts in magnitude and velocity dispersion as in the above step, we derive the best-fitting FP coefficients and compared them to the *reference* FP coefficients. The guess values of a, b, c and s_{σ_0} are changed until the best-fitting simulated FP matches the *reference* relation. In practise, we are able to match the simulated and *reference* coefficients at better than 2 per cent for both the $\log \sigma_0$ and orthogonal regressions.

Fig. 1 compares the distribution of the 1682 ETGs with available σ_0s from SDSS in sample C with that of data points for one of the toy samples, showing the similarity of the two distributions. The above procedure allows us to create simulated samples in the space of $\log r_e$, $\langle\mu\rangle_e$ and $\log \sigma_0$ down to a (model) magnitude limit of -17.64, which is more than 2.5 mag fainter than the r-band completeness limit (-20.32) of the ETG samples of Section 3.1. The effect of any selection cut on the FP can then be estimated by computing the relative variation of FP coefficients as one applies that selection to the toy samples.

Fig. 2 plots the relative variation of FP coefficients as a function of the magnitude cut. The relative variation of a given quantity, x, out of a, b, c and s_{r_e}, is computed as $(x_{\rm cut} - x)/x$, where $x_{\rm cut}$ is the value estimated for that quantity when the cut is applied. Here, instead of using the procedure of Section 4.1, the value of c is directly derived from the fit, and the s_{r_e} is obtained as the mean absolute deviation of residuals around the plane, using the (no bias-corrected) best-fitting coefficients a, b and c. For the orthogonal fit, we see that brighter the magnitude cut, more the FP coefficients

[1] Notice that the value of -20.28 is 0.04 mag fainter than the r-band model magnitude limit of the magnitude-selected ETG sample ($^{0.07}M_r = -20.32$, see Section 2). We obtain -20.28 by adding to -20.32 the difference of evolutionary correction between the median redshift of the ETG's sample of Paper I ($z = 0.0725$) and that of sample C ($z = 0.025$). To this aim, following Bernardi et al. (2003b, hereafter BER03b), we parametrize the evolutionary correction as $-2.5Q \log(1 + z)$, where the coefficient Q is equal to $\sim$0.85 in r band, at redshift $z < 0.3$.

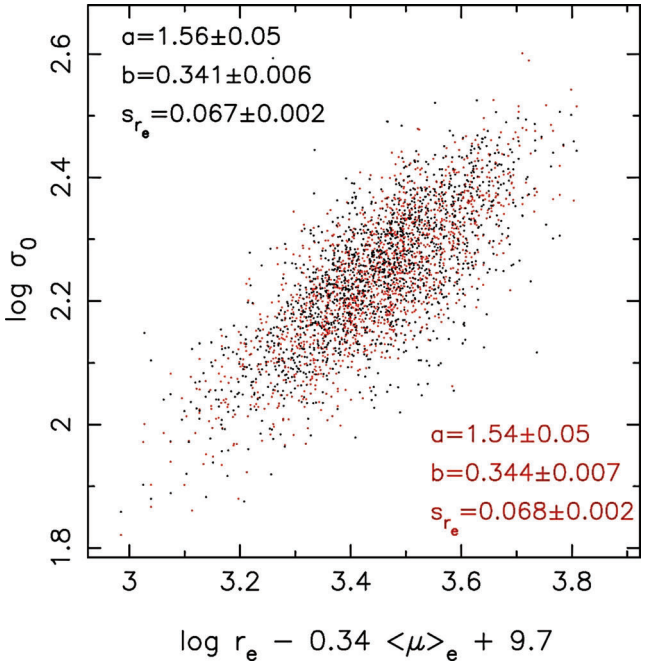

Figure 1. Comparison of the *short* edge-on projection of the FP for galaxies in sample C with available σ_0 from SDSS (black) and one toy sample (red). For both samples, only points with ${}^{0.07}M_r \leq -20.28$ and $70 \leq \sigma_0 \leq 420\,\mathrm{km\,s^{-1}}$ have been selected. The values of $\log\sigma_0$ are plotted against the variable $\log r_e – b\langle\mu\rangle_e$, i.e. the combination of photometric parameters entering the FP. The slopes (a and b) and scatter (s_{r_e}) of the relation, obtained from the $\log\sigma_0$ regression procedure, are reported in the upper left-hand and lower right-hand corners of the plot for the observed and toy samples, respectively. Notice the negligible difference between the two sets of coefficients.

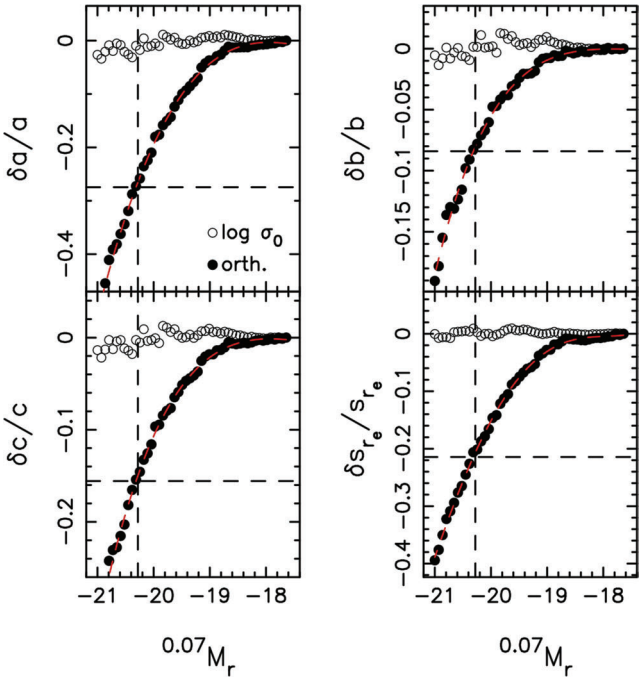

Figure 2. Relative variation of FP coefficients as a function of the magnitude cut (see the text). The variation is computed between the magnitude selected and entire toy samples. Empty and filled circles correspond to the results obtained for the $\log\sigma_0$ and orthogonal fits, respectively, as shown in lower right-hand corner of the upper left-hand panel. From left to right and top to bottom, the four panels show the relation variation (bias) in a, b, c and s_{r_e}, respectively. The vertical and horizontal dashed lines mark the completeness of the magnitude-selected sample of ETGs and the corresponding bias values, respectively. The red dashed curve in each panel is the fourth-order polynomial fit performed to model the bias as a function of ${}^{0.07}M_r$.

tend to be underestimated. This finding is consistent with that of previous studies (see LBC00; Hyde & Bernardi 2009). For the $\log\sigma_0$ fit, the FP coefficients are very insensitive, as somewhat expected, to the selection in magnitude. The vertical lines in Fig. 2 correspond to the (r-band) model magnitude limit (${}^{0.07}M_r = -20.28$) of the magnitude-selected sample of ETGs (see Section 3.1), after the small amount of luminosity evolution between $z = 0.025$ and 0.075 has been removed (see above). For that magnitude limit, the amounts of bias in a, b, c and s_{r_e} (horizontal lines) are significant, amounting to about 27, 8, 16 and 22 per cent, respectively. The same amounts of bias are also expected to affect the colour-selected samples of ETGs (see Section 3.1), whose magnitude limit in r band is very similar to that of the magnitude-selected sample. We also used the simulated samples to estimate the impact of the σ_0 cut of the ETG's sample on the FP relation. To this aim, we selected only simulated points with magnitudes brighter than ${}^{0.07}M_r = -20.28$. Applying the σ_0 selection ($70 \leq \sigma_0 \leq 420\,\mathrm{km\,s^{-1}}$), we found that relative variation of FP slopes is completely negligible (<1 per cent). This is due to the fact that, for the magnitude range considered here, almost all galaxies have $\sigma_0 > 70\,\mathrm{km\,s^{-1}}$, making the σ_0 selection unimportant.

For each sample of ETGs, as defined in Section 3.1, we consider the corresponding 2DPHOT r-band magnitude limit. For the magnitude- and colour-selected subsamples, these limits amount to −20.55 and −20.6, respectively. The 2DPHOT magnitude limit is translated to a (model) magnitude limit by adding the term 0.23 mag which is the difference of 2DPHOT and SDSS completeness magnitudes (Section 2). For a given sample, the amount of bias on a and b is then estimated evaluating the trends in Fig. 2 for the r-band model magnitude limit of that sample. This is done only for the orthogonal regression procedure, by modelling the trends in Fig. 2 with fourth-order polynomials. The biased values of a and b are multiplied by the estimated $x/x_{\rm cut}$ factors. Notice that the same correction factor is applied to all the *grizYJHK* wavebands (see also Section 7.1). The bias-corrected values of a and b are used to estimate c and s_{r_e} (Section 4.1). Fig. 3 shows how the values of c and s_{r_e} vary as a function of the magnitude limit, when this procedure is applied, rather than estimating c and s_{r_e} from the fit, as in Fig. 2. As stated in Section 4.1, the estimates of c and s_{r_e} from the bias-corrected values of a and b are almost insensitive, within ∼2 per cent, to the magnitude selection.

4.3 Bias due to correlated errors on r_e and $\langle\mu\rangle_e$

Another possible source of bias on FP coefficients is the correlation of uncertainties on $\log r_e$ and $\langle\mu\rangle_e$. As shown in Paper I, the errors on effective parameters mainly depend on the signal-to-noise ratio per pixel of galaxy images, and are slightly larger in the NIR than in the optical wavebands. For instance, the median value of the $\log r_e$ uncertainties increases from ∼0.09 in g band to ∼0.14 in K band. This variation might imply a spurious dependence of FP coefficients on waveband, and thus we have to correct the FP slopes separately in each band.

The corrections are estimated by (1) constructing simulated samples of data points in the space of $\log r_e$, $\langle\mu\rangle_e$ and $\log\sigma_0$, resembling

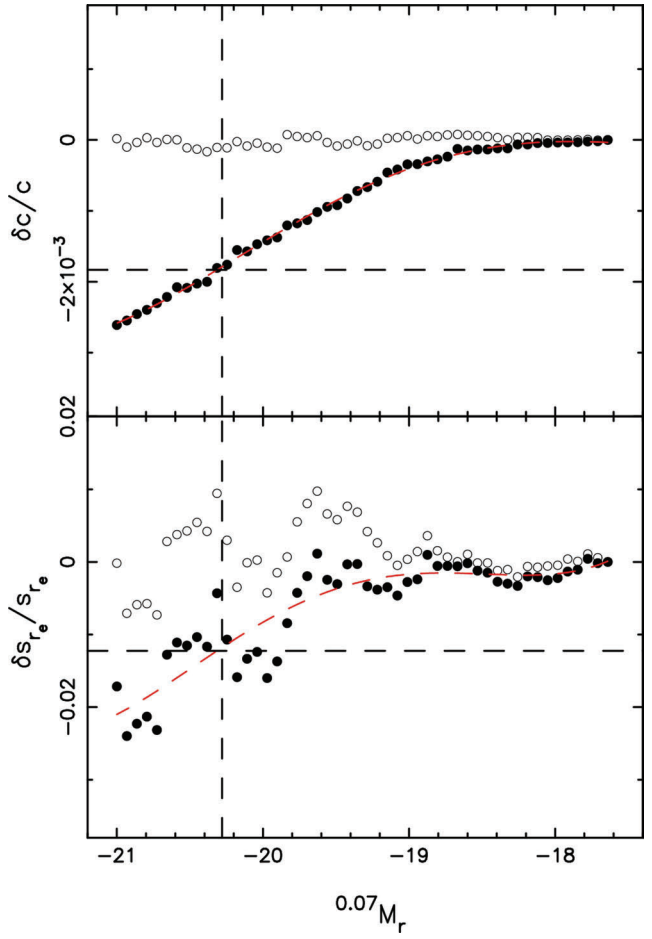

Figure 3. Relative variation of the FP offset (upper panel) and scatter (lower panel) as a function of the magnitude cut, as estimated from the toy FP samples. The offset, c, and scatter, s_{r_e}, are estimated from the bias-corrected FP slopes. Empty and filled circles correspond to the $\log\sigma_0$ and orthogonal fit values, respectively. The red dashed lines show a fourth-order polynomial fit of the filled circles. The vertical and dashed lines mark the completeness of the magnitude-selected ETG sample and the corresponding expected bias values. Notice that the bias is negligible for both quantities, being smaller than ∼2 per cent.

the distribution that galaxy's parameters would have in that space if no correlated errors on r_e and $\langle\mu\rangle_e$ would be present (Section 4.3.1), and (2) estimating how the FP slopes change by adding correlated uncertainties on the effective parameters of such simulated samples (Section 4.3.2). Notice that the toy samples of Section 4.2 are not suitable to apply the above procedure, since the corresponding effective parameters already include the effect of correlated errors on the effective parameters.

4.3.1 *Simulated samples with no correlated errors*

Each simulated sample is generated as follows. First, we extract $\log r_e$ values from a random deviate whose centre and width values are given by the mean (0.27 dex) and standard deviation (s_e = 0.25 dex) of the $\log r_e$ distribution of sample C. For a given $\log r_e$, we assign a $\langle\mu\rangle_e$ value by the KR:

$$\langle\mu\rangle_e = p_1 + p_2 \log r_e, \quad (2)$$

where p_1 and p_2 are the offset and slope, respectively. The values of p_1 and p_2 are derived by a robust least-squares fitting procedure for galaxies in sample C, by minimizing the absolute sum of residuals in $\langle\mu\rangle_e$ around the relation. As shown by La Barbera et al. (2003, hereafter LBM03), the KR fit is quite insensitive to the correlated errors on $\log r_e$ and $\langle\mu\rangle_e$. The fit gives $p_1 \sim 18.969$ and $p_2 \sim 1.95$, respectively. Then, we shift the values of $\langle\mu\rangle_e$ according to a normal Gaussian deviate of width 0.4 mag arcsec^{-2}, corresponding to the intrinsic dispersion in $\langle\mu\rangle_e$ of the KR (LBM03). For a given pair of $\log r_e$ and $\langle\mu\rangle_e$ values, we assign a $\log\sigma_0$ value by the FP relation (equation 1). The $\log\sigma_0$ values are shifted according to a random deviate with given width, s_0. The free parameters of this procedure, i.e. the FP slopes and offset, and the value of s_0, are chosen so that, on average, the FP coefficients of simulated samples match those of the magnitude-selected sample of ETGs, with the same iterative procedure as in Section 4.2.

4.3.2 *The effect of correlated uncertainties*

The $\log r_e$ and $\langle\mu\rangle_e$ of the simulated samples are then shifted according to a two-dimensional random deviate, whose covariance matrix terms are given by the median uncertainties on $\log r_e$ and $\langle\mu\rangle_e$ for galaxies in the magnitude-selected samples of ETGs. The procedure is repeated for each waveband, by using the corresponding median covariance matrix of uncertainties on effective parameters. We derive the FP slopes by (i) applying the correlated errors, and (ii) without applying any simulated uncertainty on the effective parameters. We indicate as δ_a and δ_b the ratios of FP slopes of case (ii) with respect to those obtained in case (i). Each toy sample includes $N = 2000$ data points, and the values of δ_a and δ_b are averaged over 300 realizations. The values of δ_a and δ_b in *grizYJHK* bands, for both the orthogonal and $\log\sigma_0$ regression procedures, are reported in Table 3. The correlated uncertainties on effective parameters tend to increase the value of the $\log\sigma_0$ slope of the FP, and decrease the coefficient of the $\langle\mu\rangle_e$ term. The effect is quite small, in particular for the coefficient a, amounting to less than a few per cent. The bias is larger for b, and varies almost by a factor of 2 from the optical to the NIR wavebands. Moreover, unlike the bias due to selection effects, it affects both the orthogonal and $\log\sigma_0$ regression procedures. Because of the large number of galaxies in the SPIDER sample, the factors in Table 3 are not negligible with respect to the typical errors on FP slopes (see Section 7.1). Hence, we correct the slopes of the FP in each band multiplying them by the corresponding δ_a and δ_b factors in Table 3. We have also performed some tests to check how robust the values of δ_a and δ_b are with respect to the procedure outlined above. First, one can notice that the adopted slope of the KR ($p_2 = 1.95$) is smaller than that of $p_2 \sim 3$ found by other studies (see LBM03 and references therein) and by that reported for the SPIDER samples in Section 5. Hence, we

Table 3. Effect of the correlated uncertainties of effective parameters on the slopes of the FP in different wavebands.

	Orthogonal fit		$\log\sigma_0$ fit	
Waveband	δ_a	δ_b	δ_a	δ_b
g	0.995	1.038	0.984	1.039
r	0.990	1.035	0.980	1.035
i	0.996	1.031	0.992	1.031
z	0.986	1.043	0.975	1.043
Y	0.992	1.040	0.980	1.039
J	0.985	1.060	0.977	1.062
H	0.980	1.066	0.964	1.065
K	0.975	1.070	0.956	1.069

derived the offset of the KR by fixing $p_2 = 3$ and repeated the above procedure with the corresponding values of p_1 and p_2. Second, one may notice that the width value itself of the $\log r_e$ distribution, $s_e = 0.25$ dex (see above), is broadened by the measurement errors on $\log r_e$, and hence does not correspond to the intrinsic width of the $\log r_e$ distribution. To account for this effect, we repeated the above procedure by subtracting in quadrature 0.1 dex (the typical uncertainty on $\log r_e$ in r band) to the value of s_e. For both tests, we found that the variation of the δ_a and δ_b estimates in Table 3 is completely negligible, being smaller than 0.5 per cent.

4.4 Comparison of bias-corrected FP coefficients in *r* band

In order to test the above procedure for deriving the coefficients of the FP and correct them for the different sources of biases, we apply it to the control samples of ETGs (Section 3.2). In Fig. 4, we plot the corrected slopes of the r-band FP for the five control samples. For sample C, we select only those 1682 galaxies with available σ_0s from SDSS, and (model) magnitudes brighter than -20.28 (see Section 4.3). The values of a and b are also compared to those recently obtained from Hyde & Bernardi (2009), who took into account selection effects in the fitting procedure, rather than applying correction factors as we do here. For all samples, the FP slopes are corrected for the magnitude bias evaluating the polynomial curves in Fig. 2 at a (model) magnitude of $^{0.07}M_r = -20.28$. For samples D and E, this $^{0.07}M_r$ value corresponds to the magnitude limit of -20.55, after difference between model and 2DPHOT total magnitudes is taken into account (see Paper I). In order to remove the effect of correlated errors on effective parameters, the slopes of samples D and E have also been divided by the r-band correction factors reported in Table 3.[2]

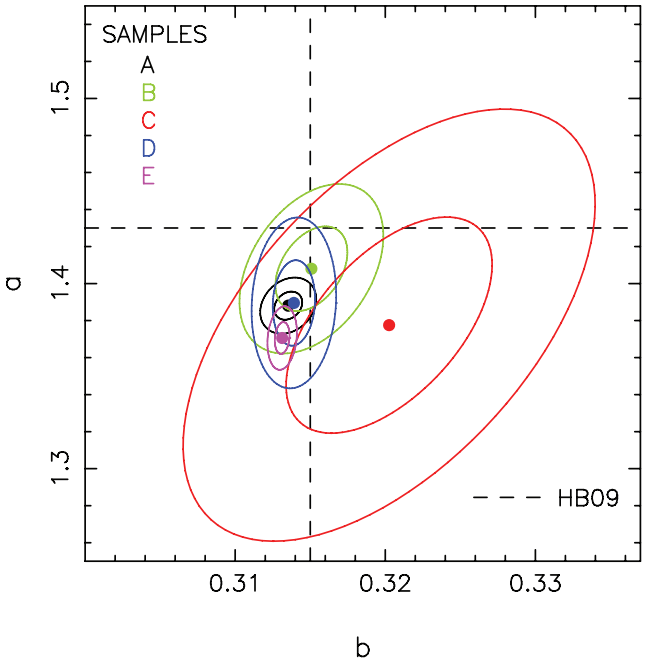

Figure 4. Slopes of the r-band FP, corrected for selection effects and correlated errors on effective parameters, for the control samples of ETGs (Table 2). Each sample is plotted with a different colour, as shown in the upper left-hand corner. For each point, the corresponding concentric ellipses denote the 1σ and 2σ confidence contours for a two-dimensional normal Gaussian deviate. The dashed lines mark the values of a and b obtained from Hyde & Bernardi (2009).

Fig. 4 shows that the FP slopes of all control samples are remarkably consistent within the 2σ level, and differ by less than $\sim$3 per cent from the values of Hyde & Bernardi (2009), proving the robustness of the procedure outlined above to derive bias-corrected FP coefficients. The consistency of FP slopes between samples A and B (D and E) shows that matching the ETG sample with UKIDSS does not lead to any significant bias in the estimate of FP coefficients, in agreement with LBM08. One can also notice that, although the SDSS and 2DPHOT effective parameters differ significantly (see Paper I), the corresponding FP relations are very consistent, as shown by the consistency of FP slopes between sample A and D (B and E). This is due to the fact that the combination of r_e and $\langle\mu\rangle_e$ that enters the FP is determined with much better accuracy that r_e and $\langle\mu\rangle_e$ themselves (see Kelson et al. 2000), making the FP relation very stable.

5 THE KORMENDY RELATION

Fig. 5 plots the r_e–$\langle\mu\rangle_e$ diagram for the colour-selected samples of ETGs (Section 3.1), from g through K. For each band, the figure also exhibits the completeness limit of the sample in that band, from Table 1. Galaxies follow a well-defined KR in all wavebands. We write the KR as in equation (2). In order to characterize the offset, p_1, the slope, p_2, and the scatter, s_{KR}, of the KR, we apply the *modified* least-squares (hereafter MLS) fitting procedure of LBM03. The MLS fit allows the coefficients of the KR to be derived by accounting for selection cuts in the r_e–$\langle\mu\rangle_e$ diagram, such as the magnitude limit. LBM03 applied three MLS fits. The $\mathrm{MLS}_{\log r_e}$ and $\mathrm{MLS}_{\langle\mu\rangle_e}$ regressions are obtained by minimizing the residuals around the relation with respect to $\log r_e$ and $\langle\mu\rangle_e$, respectively. The MLSB fit corresponds to the bisector line of the $\mathrm{MLS}_{\log r_e}$ and $\mathrm{MLS}_{\langle\mu\rangle_e}$ fits. The MLSB method is more robust and effective (i.e. lower uncertainties on fitting coefficients) with respect to the other MLS fits. For this reason, we apply here only the MLSB fit. Moreover, we generalize the MLS method to the case where orthogonal residuals around the relation are minimized. This orthogonal MLS fit (hereafter MLSO) is described in Appendix A. For both the MLSB and MLSO fits, the KR coefficients are derived accounting for the magnitude limit of the sample in the corresponding waveband. The scatter of the KR is obtained by the standard deviation of the $\log r_e$ residuals about the line, accounting for the magnitude cut as detailed in Appendix A. Fig. 5 also plots the MLSB and MLSO lines. The corresponding fitting coefficients are reported in Table 4.

From Table 4 one sees that the MLSO fit gives a larger value of the slope, p_2, with respect to the bisector fit. The scatter around the KR is independent of waveband, and larger, by $\sim$0.01 dex, for the MLSB than for the MLSO fit. The KR smoothly steepens from the g through the K band. This is shown in Fig. 6, where we plot the MLSB slope of the KR as a function of the logarithmic effective wavelength of each filter. The p_2 smoothly increase from a value of $\sim$3.44 in g to 3.8 in K. A similar trend is also observed for the results of the MLSO fit.

[2] We also estimated the uncertainties on SDSS PHOTO parameters in the same way as for the 2DPHOT effective parameters, i.e. by comparing the values of r_e and $\langle\mu\rangle_e$ from SDSS in r and i bands (see Paper I). For these uncertainties, we found that the r-band correction factors on FP slopes are even smaller than those reported in Table 3. Hence, we decided not to apply any further correction factor to samples A, B and C.

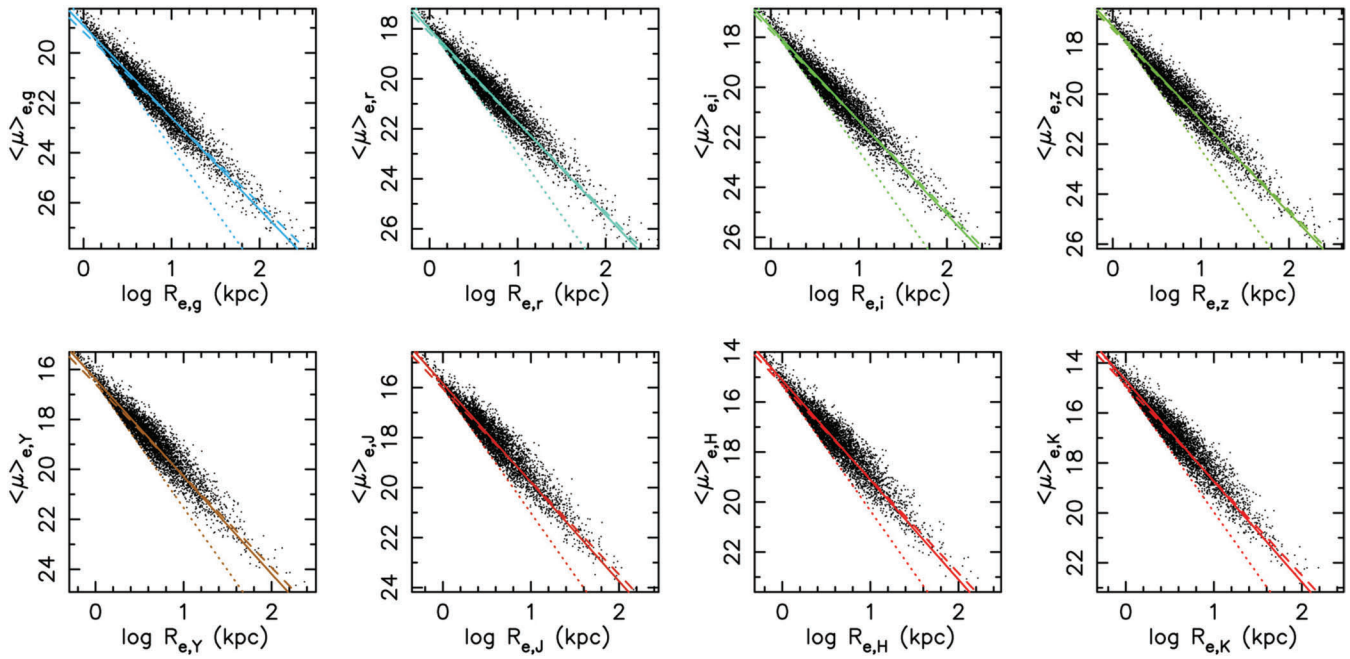

Figure 5. KR of ETGs in the *grizYJHK* wavebands (from left to right and top to bottom). For each panel, the dotted line marks the completeness magnitude in the corresponding waveband. The solid and dashed lines are the best-fitting relations obtained by the orthogonal and bisector fitting methods, respectively (see the text).

Table 4. Coefficients of the KR in *grizYJHK*.

Band	p_1	p_2 MLSB fit	s_{KR}	p_1	p_2 MLSO fit	s_{KR}
g	19.16 ± 0.04	3.44 ± 0.04	0.126 ± 0.002	18.92 ± 0.02	3.68 ± 0.02	0.115 ± 0.001
r	18.16 ± 0.02	3.55 ± 0.02	0.120 ± 0.002	18.02 ± 0.02	3.72 ± 0.03	0.114 ± 0.001
i	17.74 ± 0.02	3.60 ± 0.02	0.122 ± 0.002	17.60 ± 0.02	3.74 ± 0.02	0.117 ± 0.002
z	17.42 ± 0.02	3.61 ± 0.02	0.121 ± 0.002	17.29 ± 0.02	3.73 ± 0.03	0.116 ± 0.002
Y	16.59 ± 0.02	3.67 ± 0.02	0.125 ± 0.002	16.39 ± 0.02	3.90 ± 0.03	0.117 ± 0.001
J	16.03 ± 0.02	3.72 ± 0.02	0.126 ± 0.002	15.84 ± 0.02	3.95 ± 0.02	0.117 ± 0.002
H	15.31 ± 0.02	3.77 ± 0.02	0.126 ± 0.002	15.13 ± 0.02	3.99 ± 0.03	0.119 ± 0.001
K	14.91 ± 0.02	3.80 ± 0.02	0.128 ± 0.002	14.70 ± 0.02	4.04 ± 0.03	0.119 ± 0.001

In order to analyse the trend of p_2 with waveband, we follow the same approach as in La Barbera et al. (2004). Given two wavebands, X and W (X, W = *grizYJHK*), one can relate the corresponding slopes of the KR, $p_{2,X}$ and $p_{2,W}$, through the following equation:

$$p_{2,X} = \frac{(p_{2,W} + 5\Delta_{XW}) - \zeta(5 - p_{2,W})}{1 + \Delta_{XW}}, \quad (3)$$

where Δ_{XW} is the slope of the $X - W$ versus W CM relation, and ζ parametrizes the variation of the mean logarithmic ratio of X to W effective radii, $\log(r_{e,W}/r_{e,X})$, as a function of r_e:

$$\log \frac{r_{e,W}}{r_{e,X}} \propto \zeta \log r_{e,X}. \quad (4)$$

We first consider the case where the mean ratio of effective radii does not change along the sequence of ETGs, i.e. $\zeta = 0$. Setting $X = K$ and $W = g$, using the value of Δ_{gK} from Paper I (0.034 ± 0.016) and the value of $p_{2,g}$ of the MLSB fit, equation (3) would imply $p_{2,K} = 3.53 \pm 0.02$. This value is significantly smaller than that reported in Table 4 (3.80 ± 0.02), implying that the assumption $\zeta = 0$ is incorrect. Indeed, inverting equation (3) and using the MLSB values of $p_{2,g}$ and $p_{2,K}$, one obtains $\zeta = -0.19 \pm 0.02$. The negative sign of ζ implies that galaxies with smaller $r_{e,K}$ tend to have, on average, larger $(r_{e,g}/r_{e,K})$ value. In other terms, the NIR light profile of ETGs is more concentrated in the centre with respect to the optical for small (relative to larger) galaxies. The dependence of $(r_{e,g}/r_{e,K})$ on $r_{e,K}$ can be directly analysed by binning the SPIDER sample with respect to $r_{e,K}$ and computing the median value of $(r_{e,g}/r_{e,K})$ in each bin. The result of this procedure is shown in Fig. 7. We clearly see that the median value of $(r_{e,g}/r_{e,K})$ decreases as $r_{e,K}$ increases, and that the trend is fully consistent with what expected from the waveband variation of the KR slope (equations 3 and 4; see dashed line in the figure). In the simplistic assumption that $(r_{e,g}/r_{e,K})$ is a good proxy for the internal colour gradient in ETGs, the increasing of KR slope from g through K would imply that smaller size ETGs have stronger (more negative) internal colour gradients than galaxies with larger r_e. This point will be further analysed in a forthcoming paper, studying the optical–NIR colour gradients in the SPIDER sample (see also La Barbera & de Carvalho 2009) and their correlations with galaxy properties.

The slope of the MLSB fit can be compared to that obtained from LBM03 for a sample of ETGs in clusters at intermediate redshifts, from $z \sim 0$ to ~ 0.64. Using the MLSB fit, LBM03 found $p_2 = 2.92 \pm 0.08$ in V-band rest frame. This should be compared

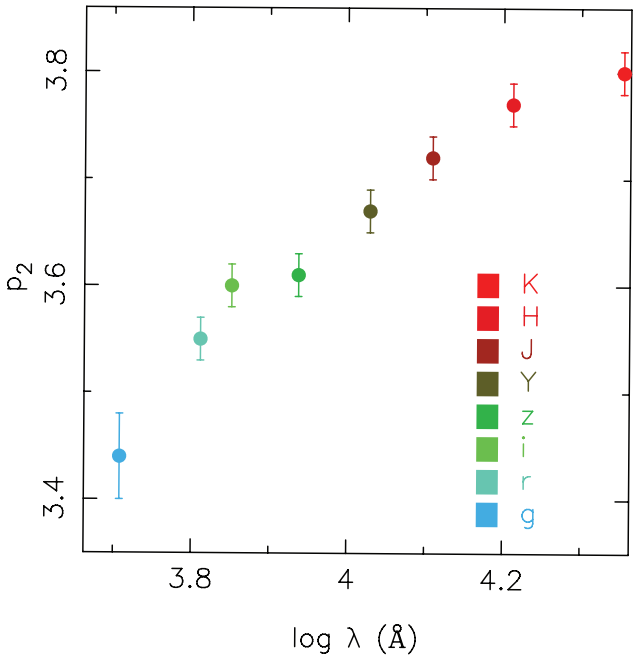

Figure 6. The slope of the KR, obtained with the MLSB fit, p_2, is plotted as a function of the logarithmic effective wavelength, $\log \lambda$, of the passbands where effective parameters are measured.

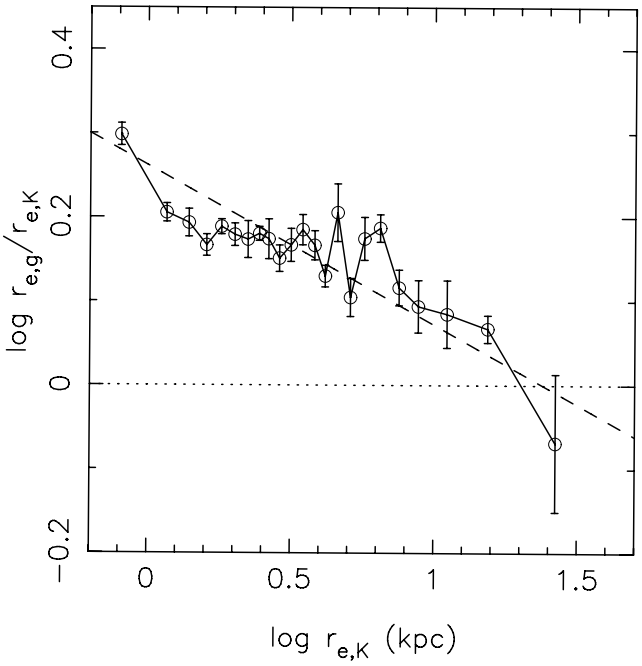

Figure 7. Logarithmic ratio of g- to K-band effective radii as a function of $\log r_e$ in K band. The solid line connects the data points obtained by median binning the distribution of $\log r_{e,g}/r_{e,K}$ with respect to $\log r_{e,K}$, with each bin including the same number ($N = 200$) of points. The trend is fully consistent with that expected from the variation of KR slope from g to K (dashed line). The dotted line marks the value of zero. Error bars denote 1σ errors on median values in different bins.

with the value of $p_2 = 3.44 \pm 0.04$ we obtain for the SPIDER sample in the g band (see Table 4), which matches approximately V-band rest frame. The slope of LBM03 is significantly flatter, by ∼15 per cent, that that we find here. One should notice that LBM03 selected ETGs by a cut in the Sersic index n ($n > 2$), while ETGs are defined here according to several photometric and spectroscopic criteria. Moreover, ETGs in the SPIDER sample reside in a wide range of environments, while ETGs in LBM03 mostly belong to rich galaxy clusters. Both these issues might be responsible for the above difference of KR slope values.

6 THE FABER–JACKSON RELATION

We write the FJ relation as

$$\log \sigma_0 = \lambda_0 + \lambda_1(\log L + 0.4X), \quad (5)$$

where λ_0 and λ_1 are the offset and slope of the relation, and X is the magnitude limit in a given waveband (see Table 1). According to this notation, the coefficient λ_0 is the $\log \sigma_0$ value predicted from the FJ relation for galaxies of magnitude X. The galaxy luminosity, L, is defined as $10^{-0.4\times{}^{0.07}M}$, where ${}^{0.07}M$ is the 2DPHOT absolute magnitude in the given band. In order to derive the coefficients λ_0 and λ_1 we use the colour-selected samples of ETGs (Section 3.1). Fig. 8 plots the distributions of ETGs in the $\log \sigma_0$ versus $\log L$ diagrams. Each sample is binned in $\log \sigma_0$, and the peak value of the $\log L$ distribution in a given bin is computed by the bi-weight statistics (Beers, Flynn & Gebhardt 1990). Since all colour-selected samples are magnitude complete, the binning procedure produces unbiased estimates of the average $\log L$ value as a function of $\log \sigma_0$. The binned values of $\log L$ versus $\log \sigma_0$ are then fitted with an orthogonal least-squares fitting procedure. For each band, the fit is performed over a fixed luminosity range of one decade, with $-0.4X \leq \log L \leq -0.4X + 1$. Uncertainties on λ_0 and λ_1 are estimated by $N = 500$ bootstrap iterations, shifting each time the $\log L$ binned values according to their error bars. The values of λ_0 and λ_1 in *grizYJHK* bands are reported in Table 5, along with the $\log \sigma_0$ scatter of the relation, σ_{FJ}, and its intrinsic dispersion, σ^{i}_{FJ}. The scatter is estimated as follows. For each bootstrap iteration, we calculate the rms of the $\log \sigma_0$ residuals through the median absolute deviation estimator. The mean value and the standard deviation of the rms values among the different iterations provide the σ_{FJ} and its error. The intrinsic scatter is computed by a similar procedure, subtracting in quadrature, for each iteration, the amount of dispersion due to the uncertainties on $\log L$ and $\log \sigma_0$ from the rms values. Considering the uncertainties, the slopes of the FJ relations are consistent among the different wavebands, with the mean value of λ_1 amounting to 0.198 ± 0.007. Using the magnitude- rather than the colour-selected samples of ETGs, this result does not change, with the value of λ_1 varying from 0.192 ± 0.018 to 0.209 ± 0.018 in r band, and from 0.220 ± 0.023 to 0.216 ± 0.032 in K band. Using STARLIGHT $\log \sigma_0$ values would also not change significantly the λ_1 values, with the mean value of λ_1 varying from 0.198 ± 0.007 to 0.187 ± 0.007. For what concerns the intrinsic dispersion around the FJ relation, it smoothly decreases by ∼0.008 dex from g through K, with a value of ∼0.091 dex in the optical and ∼0.083 dex in K band. Fixing the slope of the FJ relation in all wavebands to the average value of $\lambda_1 = 0.198$ would make this amount of variation to be 0.017 dex rather than 0.008 dex. Subtracting in quadrature the values of σ^{i}_{FJ} between the g and K bands, one obtains a value of ∼0.037 dex (i.e. ∼9 per cent in σ_0).

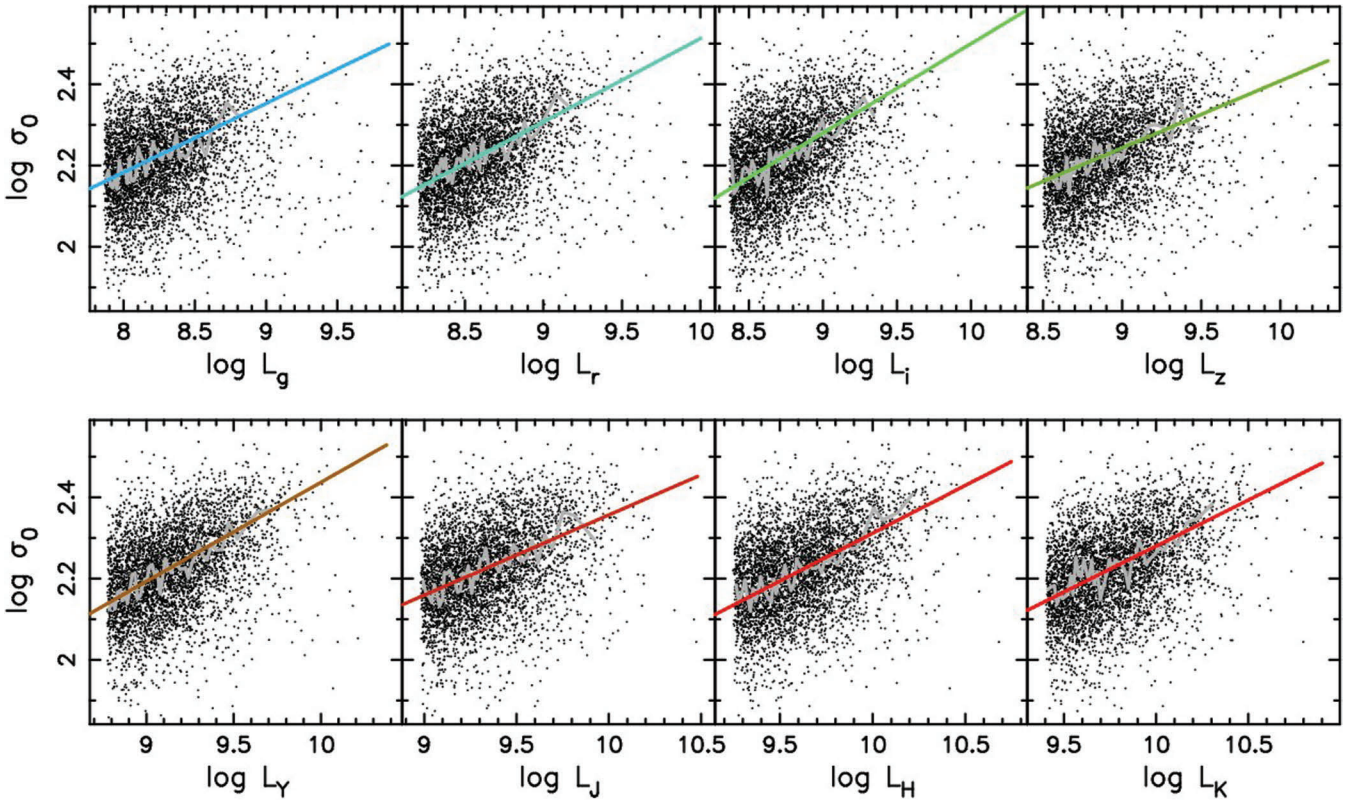

Figure 8. The FJ relation of ETGs in the *grizYJHK* wavebands (from left to right and top to bottom). For each panel, the grey curve is obtained by binning the data with respect to $\log L$, with each including the same number ($N = 40$) of galaxies. For each bin, the bi-weight peak of the $\log \sigma_0$ distribution is computed. Coloured lines show the orthogonal fit to the binned data.

Table 5. Coefficients of the FJ relation in *grizYJHK*.

Band	λ_0	λ_1	$\sigma_{\rm FJ}$	$\sigma^{\rm i}_{\rm FJ}$
g	2.158 ± 0.008	0.172 ± 0.018	0.097 ± 0.002	0.091 ± 0.002
r	2.151 ± 0.008	0.192 ± 0.018	0.096 ± 0.002	0.090 ± 0.002
i	2.155 ± 0.008	0.185 ± 0.016	0.093 ± 0.002	0.087 ± 0.002
z	2.158 ± 0.008	0.172 ± 0.018	0.097 ± 0.002	0.091 ± 0.002
Y	2.144 ± 0.007	0.217 ± 0.016	0.094 ± 0.002	0.087 ± 0.009
J	2.168 ± 0.008	0.194 ± 0.022	0.091 ± 0.002	0.084 ± 0.002
H	2.140 ± 0.008	0.233 ± 0.018	0.091 ± 0.002	0.084 ± 0.002
K	2.143 ± 0.009	0.220 ± 0.023	0.090 ± 0.002	0.083 ± 0.002

The slope value of the *r*-band FJ relation is close, but flatter, than that of 0.25 reported by Bernardi (2007) (see their equation 2). This difference can be explained by the fact that we use Sersic (rather than de Vaucouleurs) total magnitudes and by the small systematic effect in SDSS model magnitudes (see Paper I). As shown in Paper I, both effects make 2DPHOT total magnitudes to be shifted toward brighter values with respect to SDSS model magnitudes. The amount of shift is larger for bright than faint galaxies, producing a flatter FJ relation. The difference might also be related to the fact that the slope of the FJ relation seems to change according to the magnitude range where galaxies are selected (see e.g. Matković & Guzmán 2005). The slope value of the *K*-band relation, $\lambda_1 \sim 0.23$, is fully consistent with the value of 0.24 reported by Pahre, de Carvalho & Djorgovski (1998b). For what concerns the intrinsic dispersion, we find a value of $\sigma^{\rm i}_{\rm FJ} \sim 0.09$ dex in the optical, while Bernardi (2007), find a smaller value of ∼0.07 dex.

7 FP SLOPES

7.1 Variation from *g* through *K*

Because of the large sample size and the wide wavelength baseline provided by SDSS+UKIDSS, we can establish the waveband dependence of the FP with unprecedented accuracy. Fig. 9 plots the slopes of the FP in different wavebands, obtained for the magnitude- and colour-selected subsamples of ETGs (Section 3.1). In each case, we show the results of both the $\log \sigma_0$ and orthogonal regression procedures.

The slopes of the orthogonal fit are corrected for the magnitude cut bias as described in Section 4.2. In the *r* band, the 2DPHOT magnitude limit of the magnitude- and colour-selected samples of ETGs are −20.55 and −20.60, respectively. We convert these values to model magnitude limits in *r* band at redshift $z \sim 0.025$, and

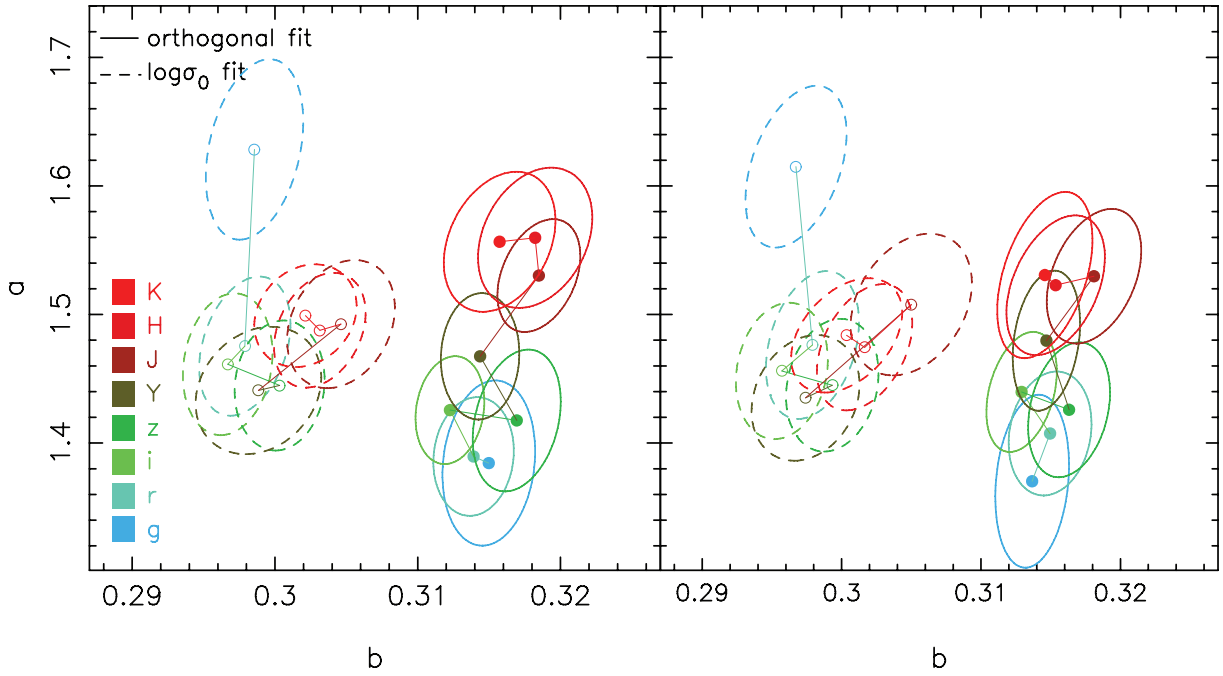

Figure 9. The $\log\sigma_0$ slope, a, of the FP is plotted against the $\langle\mu\rangle_e$ slope b. The left-hand panel shows the case where the same sample of ETGs is used to derive the FP in all wavebands, while the right-hand panel exhibits the results obtained for the colour-selected samples (see Section 3.1). In each panel, different colours denote different wavebands as shown in the lower left-hand corner of the figure. Filled and empty symbols mark the results of the orthogonal and $\log\sigma_0$ fits, respectively, with dashed and solid ellipses corresponding to 1σ confidence contours.

Table 6. Coefficients of the FP in *grizYJHK* from the orthogonal fit for the magnitude-selected sample of ETGs.

Band	a	b	c	s_{r_e}	$s^i_{r_e}$
g	1.384 ± 0.024	0.315 ± 0.001	-9.164 ± 0.079	0.125 ± 0.002	0.095 ± 0.003
r	1.390 ± 0.018	0.314 ± 0.001	-8.867 ± 0.058	0.112 ± 0.002	0.082 ± 0.002
i	1.426 ± 0.016	0.312 ± 0.001	-8.789 ± 0.053	0.110 ± 0.002	0.079 ± 0.002
z	1.418 ± 0.021	0.317 ± 0.001	-8.771 ± 0.072	0.111 ± 0.002	0.079 ± 0.003
Y	1.467 ± 0.019	0.314 ± 0.001	-8.557 ± 0.058	0.107 ± 0.002	0.081 ± 0.002
J	1.530 ± 0.017	0.318 ± 0.001	-8.600 ± 0.060	0.111 ± 0.001	0.083 ± 0.002
H	1.560 ± 0.021	0.318 ± 0.002	-8.447 ± 0.077	0.117 ± 0.002	0.087 ± 0.003
K	1.552 ± 0.021	0.316 ± 0.002	-8.270 ± 0.076	0.118 ± 0.002	0.089 ± 0.002

Table 7. Coefficients of the FP in *grizYJHK* from the $\log\sigma_0$ fit for the magnitude-selected sample of ETGs.

Band	a	b	c	s_{r_e}	c'	s'_{r_e}	δ_{r_e}	$s^i_{r_e}$
g	1.615 ± 0.032	0.297 ± 0.002	-9.275 ± 0.095	0.135 ± 0.002	-9.080 ± 0.002	0.128 ± 0.002	0.080 ± 0.001	0.100 ± 0.002
r	1.476 ± 0.029	0.298 ± 0.002	-8.726 ± 0.083	0.112 ± 0.001	-8.813 ± 0.002	0.115 ± 0.001	0.075 ± 0.001	0.087 ± 0.002
i	1.456 ± 0.027	0.296 ± 0.002	-8.517 ± 0.074	0.107 ± 0.001	-8.694 ± 0.002	0.111 ± 0.001	0.075 ± 0.001	0.082 ± 0.002
z	1.445 ± 0.026	0.299 ± 0.002	-8.477 ± 0.073	0.104 ± 0.001	-8.605 ± 0.002	0.108 ± 0.001	0.075 ± 0.001	0.078 ± 0.002
Y	1.435 ± 0.025	0.297 ± 0.002	-8.164 ± 0.073	0.099 ± 0.001	-8.353 ± 0.002	0.105 ± 0.001	0.066 ± 0.001	0.081 ± 0.002
J	1.508 ± 0.028	0.305 ± 0.002	-8.308 ± 0.085	0.103 ± 0.001	-8.195 ± 0.002	0.102 ± 0.001	0.062 ± 0.001	0.081 ± 0.002
H	1.474 ± 0.025	0.302 ± 0.002	-7.966 ± 0.074	0.105 ± 0.001	-7.991 ± 0.002	0.106 ± 0.001	0.068 ± 0.001	0.082 ± 0.002
K	1.484 ± 0.023	0.300 ± 0.002	-7.844 ± 0.072	0.106 ± 0.001	-7.872 ± 0.002	0.107 ± 0.001	0.067 ± 0.001	0.082 ± 0.002

then estimate the corresponding correction factors on a and b from the polynomial curves in Fig. 2. Since we have selected either the same sample of ETGs at all wavebands, or ETG's samples with *equivalent* magnitude limits (i.e. colour-selected samples, see Section 3.1), we apply the same correction factors to all the *grizYJHK* wavebands. Therefore, although the values of FP coefficients in a given band depend on the correction factors, their relative variation from g through K is essentially independent of them. For the $\log\sigma_0$ fitting method, which is not affected from the magnitude cut (see Section 4.2), no correction is applied. For both fitting methods, the slopes are also corrected for the (small) effect of correlated errors on effective parameters (Section 4.3), using the correction factors in Table 3. For the magnitude-selected sample of ETG, the corrected values of FP slopes are listed in Tables 6 and 7 for the orthogonal and $\log\sigma_0$ regression procedures, respectively. In Table 6, a and b are the slopes, c and s_{r_e} are the offset and the $\log r_e$ dispersion of

the FP. Error bars denote 1σ standard errors. The quantity $s^{\rm i}_{r_{\rm e}}$ is the intrinsic dispersion of the relation along $\log r_{\rm e}$. In Table 7, a and b are the slopes, c and $s_{r_{\rm e}}$ are the offset and the $\log r_{\rm e}$ dispersion of the FP. Error bars denote 1σ standard errors. The quantities c and $s'_{r_{\rm e}}$ are the offset and the scatter of the FP remeasured by fixing the values of a and b in all wavebands. The quantity $\delta_{r_{\rm e}}$ is the amount of dispersion in the $\log r_{\rm e}$ direction around the plane due to measurement errors on effective parameters and velocity dispersion, while $s^{\rm i}_{r_{\rm e}}$ is the intrinsic scatter of the FP along the $\log r_{\rm e}$ axis. For the colour-selected samples, the coefficients are very similar to those obtained for the magnitude-selected samples, and are not reported here. These tables show how small the statistical uncertainties on FP slopes are, amounting to only a few per cent in all wavebands. Notice that the large number of ETGs makes the NIR FP coefficients to have a much better accuracy than any previous study.

Both the magnitude- and colour-selected samples of ETGs exhibit very similar trends in Fig. 9. For the $\log\sigma_0$ fit, we do not see any systematic variation of the FP with waveband. From r through K, the values of a are consistent at less than 2σ. In g band, the $\log\sigma_0$ slope is larger than that in the other bands. The difference between g- and r-band values of a is significant at $\sim3\sigma$, after the corresponding uncertainties are taken into account.[3] For what concerns the coefficient b, all the values are very consistent. On the contrary, the orthogonal regression exhibits a clear, though small, variation of the slope a from g through K. The value of a is found to vary from $\sim$1.38 in g to $\sim$1.55 in K, implying a 12 per cent variation across the *grizYJHK* wavebands. The coefficient b does not change with waveband. We analysed if these results can be affected by the (small) contamination of the SPIDER sample from early-type spirals. In Paper I, we showed that the contamination from such systems is expected to be $\sim$13 per cent. We also defined a subsample of ETGs with a lower contamination of $\sim$5 per cent. Fig. 10 compares the FP slopes of the magnitude-selected sample with those obtained by selecting only galaxies in the lower contamination subsample. The values of a are fully consistent between the two cases in all wavebands, while there is only a marginally significant ($\sim2\sigma$) difference in b.

The values of a and b in Table 6 can be compared with those obtained from previous studies using the orthogonal fitting procedure. The r-band value of a is consistent, at 2σ, with that of $a = 1.49 \pm 0.05$ found by BER03b, and with the value of $a \sim 1.434$ reported by Hyde & Bernardi (2009). The value of a is larger, at the 2σ level, than that of $a = 1.24 \pm 0.07$ found by JFK96. As noticed by BER03b, the origin of such difference is still not understood, although one may notice that it further reduces when considering the value of $a = 1.31 \pm 0.07$ found from JFK96 for ETGs in the Coma cluster. For what concerns the coefficient b of the FP, its value in r band ($\sim$0.314) is consistent with that of 0.328 ± 0.008 found by JFK96, and with the value of $\sim$0.316 from Hyde & Bernardi (2009). On the other hand, BER03b report a somewhat lower value of $b = 0.300 \pm 0.004$. For what concerns the NIR FP, the values of the slopes can be compared with those obtained from Pahre et al. (1998a), who found $a = 1.53 \pm 0.08$ and $b = 0.316 \pm 0.012$, still very consistent with our findings. The finding that b does not change with waveband is in full agreement with what already suggested by Pahre et al. (1998a).

[3] To estimate the significance level, we add in quadrature the errors on a for the two wavebands, assuming they can be treated as independent uncertainties.

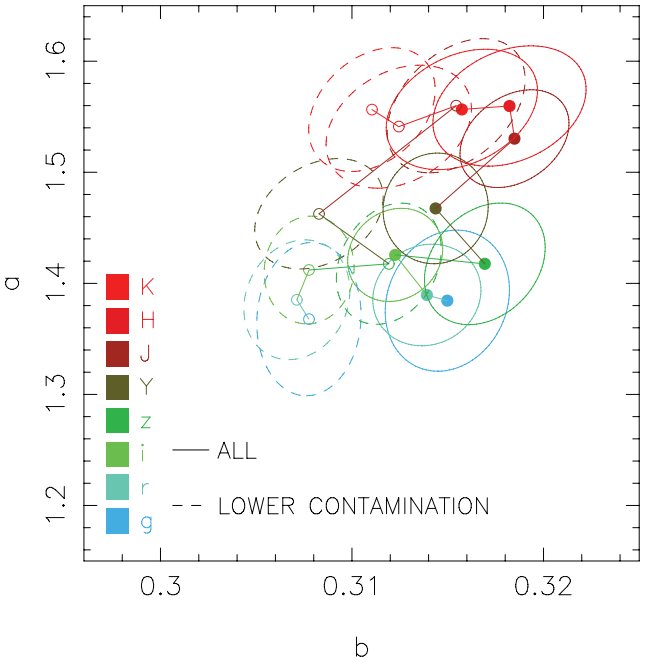

Figure 10. Effect of limiting the analysis to the sample of ETGs with lower contamination from galaxies with residual disc-like morphological features (see Paper I). Filled circles and solid ellipses refer to the results of the orthogonal fitting procedure for the magnitude-limited sample of ETGs. Dashed ellipses and empty circles are those obtained for the sample with lower contamination (see the text). Ellipses denote 2σ error contours. The FP coefficients turn out to be consistent between the two cases, from g through K.

The above results on the waveband dependence of the FP extend the findings of LBM08, who derived the FP in the r and K bands for 1400 ETGs selected with similar criteria as in the present study. For the orthogonal fit, LBM08 obtain $a = 1.42 \pm 0.05$ and $b = 0.305 \pm 0.003$ in r band, and $a = 1.53 \pm 0.04$ and $b = 0.308 \pm 0.003$ in K band. The values of a are fully consistent with those reported in Tables 6 and 7, while the values of b are smaller, at 2.5σ, than those we find here. This (small) difference is likely explained by the different correction procedure adopted here with respect to that of LBM08. In agreement with LBM08, we find that, when considering the $\log\sigma_0$ fit, one does not see any significant variation of FP slopes with waveband. When comparing the orthogonal fit results in r and K bands, LBM08 found a variation of only 8 ± 4 per cent (see the values reported in their table 1). Here, considering the r- and K-band values of a in Table 6, we find a variation of 11 ± 2 per cent. The variation is even smaller, amounting to $\sim$8.5 per cent, when considering the colour-selected samples of ETGs. Both values are consistent, within the uncertainties, with those found by LBM08.

7.2 Dependence on velocity dispersion estimates and magnitude range

As described in Paper I, two alternative velocity dispersion estimates are available for the entire sample of ETGs, those retrieved from SDSS DR6 and the new values we have measured by means of STARLIGHT (Cid Fernandes et al. 2005). Fig. 11 compares the FP slopes we derive in the different wavebands when using either one or the other set of σ_0 values. Although we find a good agreement among STARLIGHT and SDSS DR6 σ_0 values (see Paper I), the FP slopes slightly change when using either one or the other source

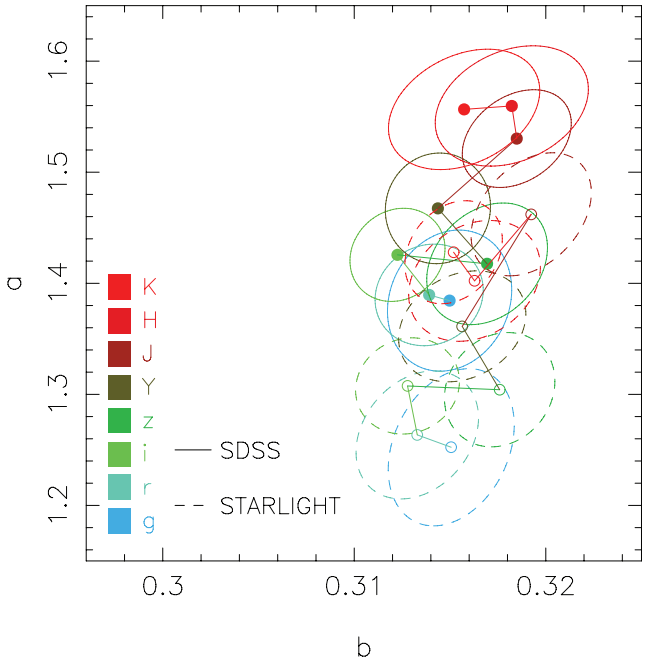

Figure 11. Effect of changing the method to derive velocity dispersions on FP slopes. Filled and empty symbols are the values of FP slopes obtained by using SDSS DR6 and STARLIGHT σ_0 values, respectively, for the magnitude-selected sample of ETGs. Solid and dashed ellipses plot 2σ confidence contours for the samples with SDSS DR6 and STARLIGHT velocity dispersions, respectively. Different colours mark different wavebands, as in Fig. 9. Notice that scales and labelling are the same as in Fig. 10.

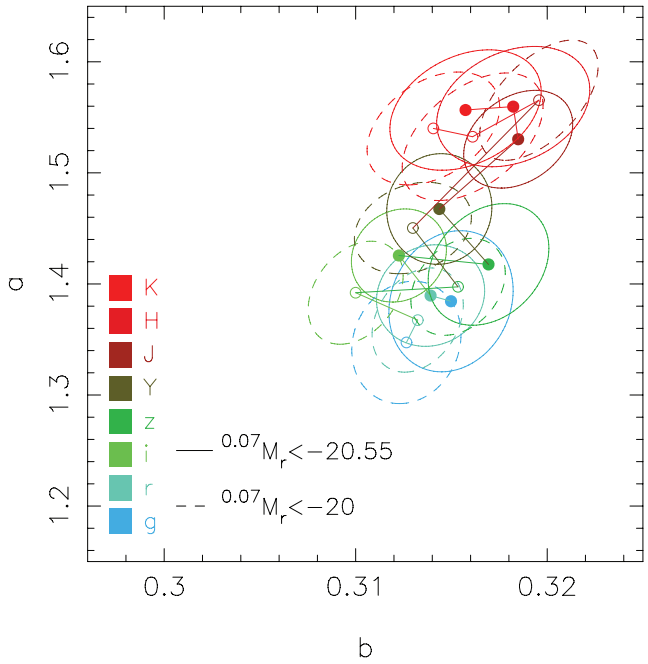

Figure 12. Same as Fig. 10 but showing the effect of using the entire SPIDER sample, rather than the magnitude-selected sample of ETGs, on the waveband dependence of the FP. Notice that scales and labelling are the same as in Fig. 10.

of σ_0s. In particular, the value of a is systematically smaller for STARLIGHT with respect to SDSS DR6. Averaging over all the wavebands, the difference amounts to ~ -9 per cent. We notice that the r-band value of $a = 1.26 \pm 0.03$ from the STARLIGHT σ_0s matches exactly the value of a obtained by JFK96 (see Section 7), implying that the method to measure the σ_0 might be one main driver of the differences in FP coefficients between BER03b and JFK96. Notice also that the value of b is essentially independent of the velocity dispersion estimates.

In order to analyse if the waveband dependence of the FP is sensitive to the magnitude range where ETGs are selected, we proceed as follows. First, we select all the ETGs in the SPIDER sample, with photometry available in *grizYJHK* and reduced χ^2 smaller than 3. This selection is the same as for the magnitude-selected sample of ETGs (Section 2), but without applying any magnitude cut in r band. The sample consists of 4981 galaxies. Fig. 12 compares the FP slopes of the magnitude-selected sample of ETGs with those obtained for the entire sample. The slopes of the FP are fully consistent in all wavebands between the two cases. We also define two subsamples consisting of all the ETGs with available photometry in *grizYJHK* and r-band magnitude brighter that $^{0.07}M_r = -21$ and -21.5, respectively. We exclude galaxies whose Sersic model fit gives an high χ^2 value (>3). These $^{0.07}M_r = -21$ and -21.5 subsamples include $N = 3411$ and 2091 galaxies, respectively. Fig. 13 compares the slopes of the FP obtained for these two samples, by the orthogonal fitting procedure, with those obtained for ETGs in the magnitude range of $^{0.07}M_r \leq -20.55$. In order to allow a direct comparison of the amounts of variation with waveband, for both subsamples, the best-fitting values of a and b are rescaled to match the values of a and b in the r band for the magnitude-selected sample. The figure clearly shows that the waveband dependence of the FP is essentially the same regardless of the magnitude range. For $^{0.07}M_r \leq -21$, the variation of a is smaller, but consistent within the errors, with that obtained for $^{0.07}M_r \leq -20.55$. For $^{0.07}M_r \leq -21.5$, the trend of a versus b matches very well that obtained for the entire sample. In all cases, the $\log \sigma_0$ coefficient increases from g through K, while the value of b is independent of waveband.

7.3 Dependence on galaxy parameters

The FP relation and its dependence on waveband might change when selecting samples of ETGs with different properties. To analyse this aspect, we split the magnitude-selected sample according to the value of different galaxy parameters, i.e. the axial ratio, b/a, the Sersic index, n, the $r - K$ colour index and the average discy/boxiness parameter, a_4. We utilize the values of b/a and n in the r band, while for a_4, we adopt its median value among the *gri* wavebands (see Paper I). The $r - K$ colour is computed from 2DPHOT total magnitudes.

Fig. 14 plots the slope a of the FP as a function of b. The slope's values are those obtained from the orthogonal fit, applying the same correction factors as for the entire sample (Section 7.1). Each panel corresponds to a given parameter p: a_4, b/a, n and $r - K$. For each parameter, the magnitude-selected sample of ETGs is splitted in two subsamples, having values of p either lower or higher than a given cut value, p_c. For $p = b/a$, n and $r - K$, we set p_c equal to the median value of the distribution of p values. The median values are $p_c = 0.699, 6.0$ and 3.0 for b/a, n and $r - K$, respectively. For a_4, we divide the sample into discy ($a_4 > 0$) and boxy ($a_4 < 0$) galaxies. Notice that, for a given parameter, galaxies in the two subsamples can populate different regions of the $\log r_e$–$\langle\mu\rangle_e$–$\log \sigma_0$ space. For instance, because of the luminosity–size relation and the KR, galaxies with higher Sersic index are brighter and tend to have higher values of $\langle\mu\rangle_e$. This *geometric* difference might

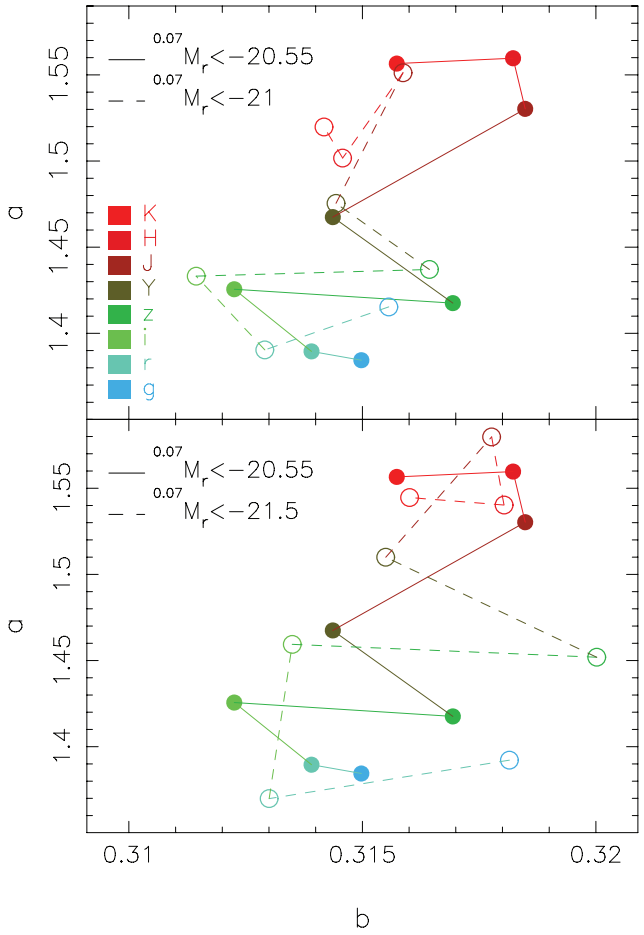

Figure 13. Effect of changing the magnitude limit on the waveband dependence of the FP. The upper and lower panels plot as open circles, connected by dashed segments, the FP slopes a and b obtained when applying different magnitude limits of ${}^{0.07}M_r = -21$ and -21.5, respectively. In both panels, the results, obtained for the entire magnitude-selected sample, are also shown, for comparison, as filled circles, connected by solid segments. Different colours mark different wavebands, as in Fig. 9.

produce spurious differences in FP coefficients. A trivial example of this geometric effect is the magnitude selection: the bias on FP coefficients changes for samples of ETGs spanning different luminosity ranges (Section 4.2). In order to minimize any geometric difference, for a given parameter p, we extract the two subsamples of ETGs by constraining their distributions in magnitude and $\langle\mu\rangle_e$ to be the same (see Appendix B for details).

Fig. 14 shows that the waveband dependence of the FP is similar for all subsamples, i.e. the value of b tends to be constant while the coefficient a increases by ∼15 per cent from g through K. However, the FP slopes change significantly for samples of ETGs with different properties. The differences can be summarized as follows.

(1) Galaxies with higher n have a lower value of b; the value of a in the NIR is smaller for the subsample with $n > 6$, while in the optical both subsamples have consistent a.

(2) The FP of round galaxies (higher b/a) is more tilted (smaller a) than that of galaxies with low b/a. The difference is more pronounced in the NIR than in the optical.

(3) For a_4 and $r - K$, one can notice a different behaviour. In the NIR, the FP slopes of the two subsamples are fully consistent, while in the optical, there is a detectable difference in the coefficient b. Boxy and blue (i.e. $r - K < 3$) galaxies tend to have lower b.

We remark that all these trends remain essentially unchanged when replacing SDSS DR6 with STARLIGHT velocity dispersions, with the exception that a is slightly lower for STARLIGHT relative to SDSS σ_0 values (see Section 7.2).

Fig. 15 shows the FP slopes obtained for different subsamples as in Fig. 14, but without imposing the constraint that, for a given quantity, the two subsamples consist of galaxies with the same distributions in magnitude and $\langle\mu\rangle_e$. No difference would have been detected with respect to n and b/a, while a (spurious) difference in the NIR value of a between red and blue galaxies would have been found. The comparison of Figs 14 and 15 proves that accounting for purely *geometric* differences in the space of FP parameters is of paramount importance to correctly analyse the scaling relations of different galaxy samples.

8 THE EDGE- AND FACE-ON PROJECTIONS OF THE FP

So far, we have analysed the waveband dependence of the FP, and that of the FJ and KR. Since the FJ and KR are projections of the FP, we expect their waveband dependence to be connected to that of the distribution of galaxies in the FP. We establish this connection by analysing the edge- and face-on projections of the FP.

Fig. 16 presents the so-called short edge-on projection of the FP, from g through K, namely the combination of effective structural parameters, $\log r_e - b\langle\mu\rangle_e$, as a function of $\log\sigma_0$. This corresponds to the FP along the *shortest* axis, whose slope is equal to its $\log\sigma_0$ coefficient, a. Each panel in Fig. 16, for a given passband, shows the FP obtained from the orthogonal fitting method (solid line), as well as the r-band fitted FP (dashed line). From these plots we can see the increasing of a from the optical through the NIR. Comparing the solid and dashed lines we see that the increasing is quite small (see Section 7.1). The observed scatter in the edge-on projection decreases from the optical through the NIR, as it can be attested from the values of the FP $\log r_e$ dispersion, s_{r_e}, reported in Table 7.[4]

In order to represent the FP face-on projection, we follow the same formalism as in Guzmán, Lucey & Bower (1993, hereafter GLB93). We project the FP into a plane defined by two orthogonal directions, one of which is perpendicular to the $\log r_e$ axis. The axes of the projection are

$$X' = (x_0 \log r_e + b' \log\langle I\rangle_e + a \log\sigma_0)/\sqrt{x_0\,(1 + x_0)}, \quad (6)$$

$$Y' = (a \log\langle I\rangle_e - b' \log\sigma_0)/\sqrt{x_0}, \quad (7)$$

where $b' = -b \times 2.5$, $x_0 = a^2 + (b')^2$ and $\langle I\rangle_e$ is the mean surface brightness in flux units, with $\langle\mu\rangle_e = -2.5 \log\langle I\rangle_e$. From the FP equation and equation (6), it follows that X' is simply proportional to $\log r_e$. Fig. 17 shows the distribution of ETGs on the face-on projection of the FP in r band, together with the $\log r_e$, $\langle\mu\rangle_e$ and $\log\sigma_0$, directions, as well as the directions of increasing total magnitude, MAG, and logarithmic luminosity, $\log L$, on the face-on FP. The dashed lines in the plot illustrate the σ_0 and magnitude selection limits of the sample (Section 2). As already noticed in previous studies (e.g. Bender, Burstein & Faber 1992; GLB93; JFK96),

[4] We actually refer to the scatter values reported in Table 7 (and not those reported in Table 6) as for the $\log\sigma_0$ fitting procedure the FP slopes do not change significantly with waveband, allowing a meaningful comparison of the s_{r_e} values from g through K.

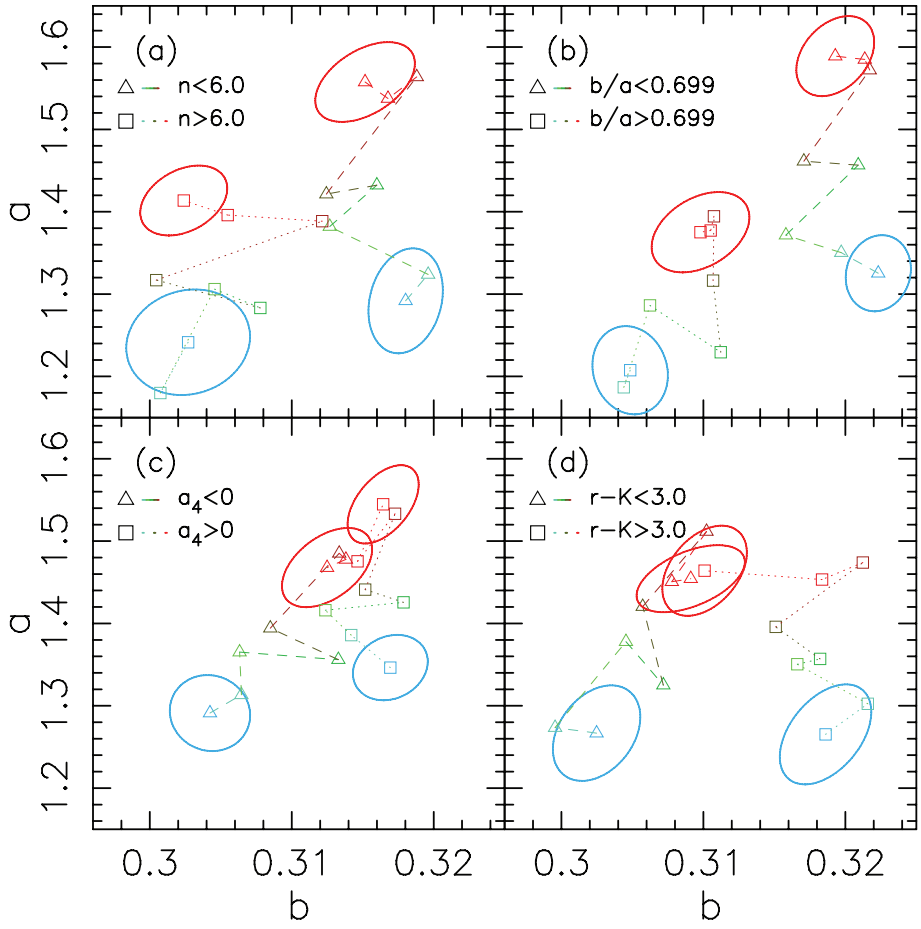

Figure 14. FP slopes, from g through K, for different subsamples of ETGs. Each panel shows the FP slopes obtained by splitting the magnitude-selected sample of ETGs in two subsamples, according to the Sersic index (a), the axial ratio (b), the isophotal parameter, a_4 (c) and the $r-K$ colour index (d). For each quantity, the two bins are defined as shown in the lower right-hand corner of the corresponding panel. The slope's values are plotted with different symbols and are connected through different line types for the two bins, as shown in lower right-hand corner of each plot. Different wavebands are represented with different colours, as in Fig. 9. Ellipses denote 1σ confidence contours for a and b. To make the plot more clear, only the ellipses in g and K bands are shown. Notice that scales and labelling of each panel are the same as in Fig. 10.

ETGs are confined in a *small* region of the face-on projection, only partly due to selection effects. Galaxies populate a diamond-shaped region, limited at low X' by the magnitude limit of the sample, $M_{r,\rm lim} = -20.55$, and at high X', by the bright-end knee of the galaxy luminosity function, i.e. the fact that there are no galaxies brighter than a magnitude threshold of about $M_{r,\rm lim} - 4$. Notice that the σ_0 selections (see Paper I and Section 2) do not affect the shape of the distribution in the face-on projection, as all galaxies lie well within the region defined by these additional cuts (dashed green lines in the figure).

Since the $\log r_{\rm e}$ and $\langle\mu\rangle_{\rm e}$ directions form almost a 90° angle on the FP (see the blue and magenta arrows in the upper right of Fig. 17), the KR is essentially reflecting the face-on distribution, as already noticed by GLB93. In order to establish this connection, we perform an orthogonal least-squares fit of the diamond-shaped region, accounting for the magnitude selection in the X'–Y' plane by the MLSO fitting procedure (see Section 5). The relation is

$$Y' = \text{const} + A'\,X', \tag{8}$$

where A' is the slope, and const is an offset. For the r band, we obtain a best-fitting value of $A' = -1.08 \pm 0.01$. Since the $\log r_{\rm e}$ and $\langle\mu\rangle_{\rm e}$ directions are approximately orthogonal, the fitted line is very similar to what we would obtain by binning the data with respect to $\log r_{\rm e}$ and take the median values of X' and Y' in each of those bins. The result of this binning procedure is shown by the magenta circles in Fig. 17. The magenta line is the best fit of the binned data points, with a slope of -1.01 ± 0.02, very close to the MLSO fit reported above. The 2σ scatter of the MLSO fit, along the X', is displayed by a segment in the lower left of Fig. 17, with the shorter segment corresponding to the 2σ $\log r_{\rm e}$ dispersion of the FP seen edge-on (Table 6). The scatter around the edge-on FP is about twice smaller than that of the face-on FP as already noticed by GLB93 implying that the FP is more like a *band* rather than a plane, in the $\log r_{\rm e}$, $\langle\mu\rangle_{\rm e}$, $\log\sigma_0$ space. We can use equation (8) to eliminate $\log\sigma_0$ from the FP equation (equation 1). This leads to a linear relation between $\langle\mu\rangle_{\rm e}$ and $\log r_{\rm e}$, similar to equation (2), i.e. the KR, whose expected slope is

$$p_2' = \frac{b}{x_0} - a\,A'\,\frac{\sqrt{1+x_0}}{0.4x_0}. \tag{9}$$

Inserting the r-band value of the FP slope from Table 6 and the best-fitting value of A' in this equation, we obtain $p_2' = 3.56 \pm 0.03$, in good agreement with the KR r-band slope, $p_2 \sim 3.55$, obtained by the MLSB fit (see Table 4).

As far as the FJ relation, we notice that the $\log L$ and $\log\sigma_0$ axes form a small angle on the FP, and are almost orthogonal to the

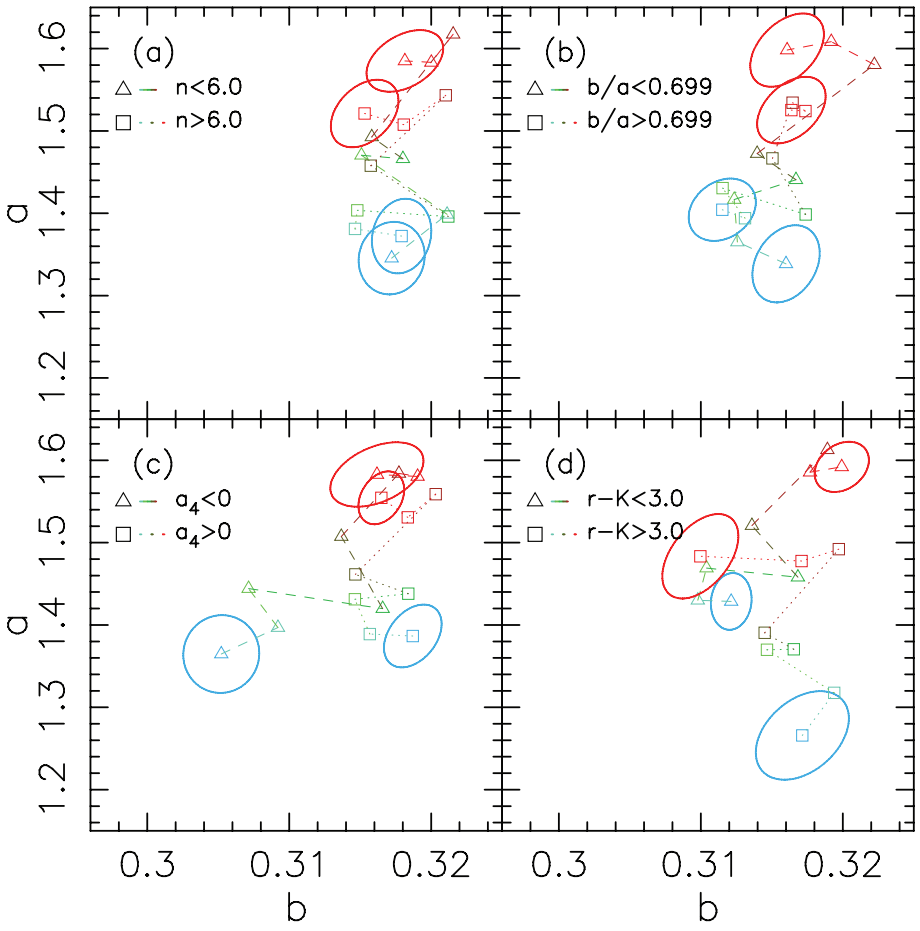

Figure 15. The same as in Fig. 14, but without matching the distributions in magnitude and mean surface brightness of subsamples in the two bins of a given quantity.

direction of the long diagonal of the diamond-shaped region. As a consequence, the best-fitting line of the face-on distribution cannot be directly connected to the FJ, as we do for the KR. In fact, the FJ relation almost coincides with the (short) edge-on projection of the FP (e.g. GLB93). In order to overcome this problem and relate the face-on distribution and the FJ relation, we bin the data with respect to $\log L$ and then compute the median values of X' and Y' in each bin. This binning procedure allows us to look at the distribution of galaxies in different luminosity bins, in the same way as for the FJ relation. The $\log L$-binned points are plotted as red circles in Fig. 17. The corresponding linear best fitting is displayed as a red line. The slope value of the red line amounts to $A'_L = -0.72 \pm 0.03$. Notice how the MLSO fit and the red line differ significantly. Replacing A' with A'_L in equation (8), and combining the resulting equation with the FP, we obtain a linear relation between $\log L$ and $\log \sigma_0$, similar to the FJ equation (equation 5), with an expected slope of

$$\lambda'_1 = \frac{a - b'\,A'_L\,\sqrt{1+x_0}}{a\,A'_L\,\sqrt{1+x_0} + b' + 2x_0}. \qquad (10)$$

Inserting the value of A'_L and the FP coefficients in this equation we obtain $\lambda'_1 = 0.14 \pm 0.01$, very close to the measured slope of the FJ relation in r band ($\lambda_1 = 0.19 \pm 0.02$, see Table 5). The difference between λ_1 and λ'_1 does not reflect any inconsistency in the data, but just the fact that the $\log L$ and $\log \sigma_0$ directions form a small angle on the FP, and hence it is not straightforward to connect the distribution of galaxies on the face-on projection to that on the $\log L$–$\log \sigma_0$ plane. Equation (10) is used here as an empirical tool to analyse the dependence of the FJ relation on waveband (see below).

Fig. 18 shows the face-on projections of the FP from g through K. For each band, we have performed an MLSO fit of the data, as well as a $\log L$-binned fit, in the same way as we do in Fig. 17. For each band, the corresponding slopes, A' and A'_L, are reported in Table 8, together with the predicted slopes of the KR, p'_2, and FJ relation, λ'_1, from equations (9) and (10), respectively. From Table 8 we see that the slope of the KR is expected to increase with waveband, in agreement with what we measure (Section 5). This can be seen directly from equation (9), as b does not change significantly with waveband, and the same holds for the term $\sqrt{1+X_0}/X_0$. It follows that the waveband dependence of the KR slope is driven by the term $-a\,A'$ (second term of equation 9). From the values of A' in Table 8, we see that $-A'$ increases with waveband, i.e. the MLSO fitted line steepens with waveband, in the same way as a does (Section 7.1). Therefore, the variation of the KR from g through K is connected to the variation of both the slope, a, and the face-on projection of the FP with waveband. The steepening of the MLSO fit from g through K can be explained by the variation of optical to NIR radii along the ETG's sequence (Section 5), and considering the fact that X' is essentially proportional to $\log r_e$.

For what concerns the FJ relation, the slope listed in Table 8 does not change with wavelength, which is consistent with the results presented in Section 6. Equation (10) explains the reason for this behaviour. First, we notice that the FP slope, a, appears both in the

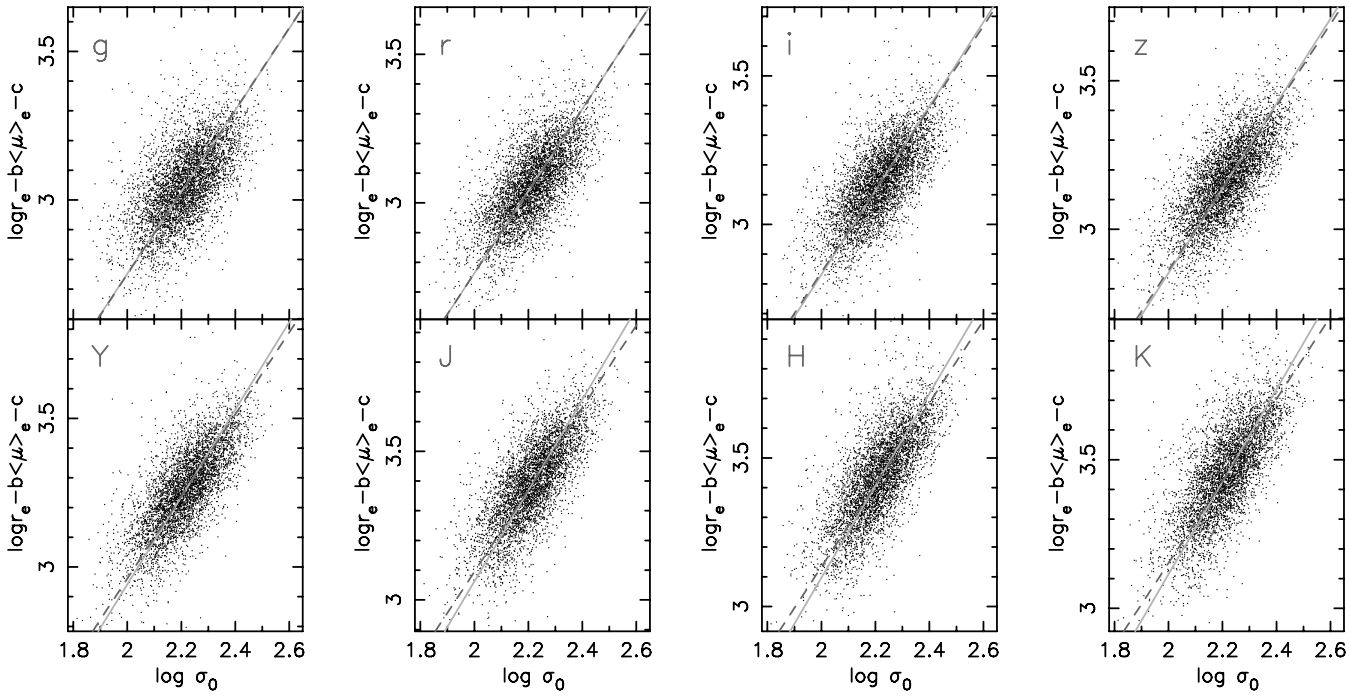

Figure 16. Short edge-on projection of the FP (see Section 8), where the photometric quantity entering the FP, $\log r_{\rm e} - b\langle\mu\rangle_{\rm e}$, is plotted against the spectroscopic quantity $\log\sigma_0$. Different panels correspond to different passbands, from *g* (upper left) through *K* (lower right), as indicated in the upper left-hand corner of each plot. In the short edge-on projection, the FP projects into a line, having a slope equal to the FP coefficient *a*. For each panel, this projection is shown by the solid light-grey line. In order to emphasize the waveband dependence of *a*, in each panel we plot as a reference, with a dashed dark-grey line, the *r*-band FP projection. Notice that the value of *b*, defining the *y*-axis variable changes among different panels, according to the values reported in Table 6. Notice that for a more direct comparison of the FP projection in different wavebands, the lengths of the *x*- and *y*-axes are the same for all panels.

upper and lower part of the second term of equation (10). Therefore, the waveband dependence of *a* does not affect the λ_1' value. Moreover, from Table 8, we see that the $\log L$-binned slope of the FP face-on distribution is *independent* of waveband, making the value of λ_1' constant from *g* through *K*. In other words, the face-on distribution of the FP changes with waveband in a complex way, so that the long diagonal of the diamond-shape region steepens with waveband, while the $\log L$-binned envelope of the distribution does not change with waveband. The former effect, together with the waveband variation of the FP coefficient, *a*, determines a dependence of the KR on waveband, while the latter is consistent with the FJ relation not changing from *g* through *K*.

9 STELLAR POPULATIONS ALONG THE FP

Under the homology assumption, one can combine the FP relation (equation 1) with the virial theorem

$$\sigma_0^2 \propto \frac{M}{L}\langle I\rangle_{\rm e} r_{\rm e}, \tag{11}$$

and parametrize the mass-to-light ratio, M/L, as a function of two variables out of $M, L, \sigma_0, r_{\rm e}$ and $\langle I\rangle_{\rm e}$ (Djorgovski, de Carvalho & Han 1988). Here, we denote as $\langle I\rangle_{\rm e}$ the mean surface brightness within $r_{\rm e}$ in flux units. In order to analyse how stellar population parameters vary along the sequence of ETGs, it is convenient to parametrize such sequence by means of variables that are independent of stellar population parameters. To this effect, we consider the quantities *M* and σ_0, and write

$$\frac{M}{L} \propto M^{\beta_x}\sigma_0^{\alpha_x}, \tag{12}$$

where the index *x* runs over all the available wavebands ($x = grizYJHK$). Using equation (1) and equation (11), one obtains the following expressions for α_x and β_x:

$$\alpha_x = 4 - 0.4\left(\frac{a_x+2}{b_x}\right), \tag{13}$$

$$\beta_x = \frac{0.4}{b_x} - 1, \tag{14}$$

where a_x and b_x are the values of the $\log\sigma_0$ and $\langle\mu\rangle_{\rm e}$ slopes of the FP in the waveband *x*. These equations imply that at fixed σ_0 the variation of the M/L with mass is completely determined by the coefficient *b* of the FP. On the contrary, at fixed *M*, the variation of M/L with velocity dispersion is determined by both the values of *a* and *b*. Hence, the result that *b* does not change from *g* through *K* (see Section 7) implies that, at fixed σ_0, the change of M/L with mass is independent of waveband. On the contrary, the dependence of M/L with σ_0 (at fixed *M*) changes from *g* through *K*. This is shown in Fig. 19 where we plot the values of α and β in the *grizYJHK* wavebands. For each band, we calculate α and β from equations (13) and 14, using the FP coefficients obtained by the orthogonal fitting procedure (see Table 6). The reason for adopting the FP slope's values from the orthogonal regression is discussed in Section 9.1. As expected, the value of β is constant, while α increases from *g* through *K*. Although the variation of *a* from *g* through *K* amounts to only ∼12 per cent, the corresponding increase in the α value is significant, amounting to ∼70 per cent.

One can also notice that the values of α and β have opposite sign. Since the value of α is negative, at a given mass, the M/L is a decreasing function of σ_0. On the contrary, for fixed σ_0, the M/L increases with *M*. In order to characterize the overall variation

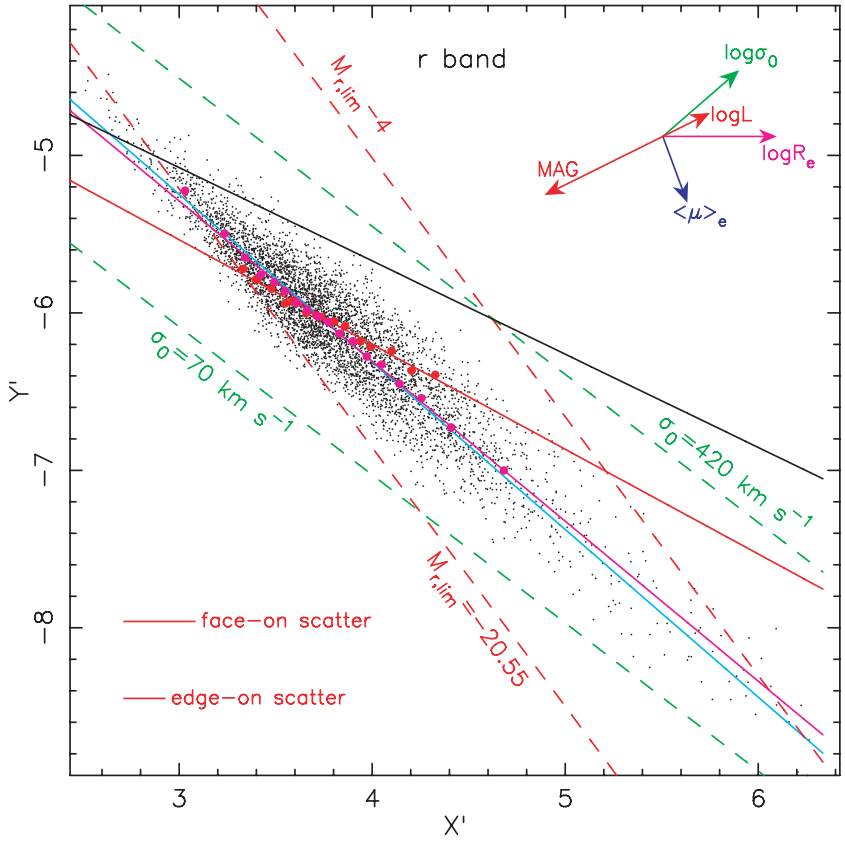

Figure 17. Face-on projection of the FP in r band. The projection is such that the x-axis variable, X', is proportional to $\log r_e$, while the y-axis variable, Y', is proportional to $-\langle\mu\rangle_e$ and $\log\sigma_0$. The arrows in the upper right-hand corner of the plot denote the directions where the quantities, MAG, $\log\sigma_0$, $\log L$, $\langle\mu\rangle_e$ and $\log r_e$ increase, where MAG is total galaxy magnitude, and $\log L$ is logarithmic luminosity in r band. The size of the arrows amounts to 0.5 dex, 1 mag arcsec^{-2}, 3 mag and 0.5 dex for $\log\sigma_0$, $\langle\mu\rangle_e$, MAG and $\log r_e$, respectively. The red dashed lines correspond to the r-band magnitude limit, $M_{r,\rm lim} = -20.55$, and a bright-end limit four magnitudes brighter than $M_{r,\rm lim}$, as shown by the corresponding labels. The green dashed lines correspond to the $\log\sigma_0$ lower and upper selection limits of 70 and 420 km s^{-1}. The solid cyan line is the MLSO best-fitting relation to the data (see the text). The thick solid black line marks the exclusion zone, $Y' = -0.59X' + \rm const$, as originally defined by Bender, Burstein & Faber (1992). The intercept of this line has been arbitrarily normalized to mark the upper envelope of the face-on projection of the FP. The presence of a few points above the line is likely due to measurement errors on FP variables. The magenta and red circles are obtained by binning the data with respect to $\log r_e$ and $\log L$, respectively, computing the median values of X' and Y' in each bin. The magenta and red solid lines are the best-fitting lines to the binned data points. The size of the 2σ scatter around the fit of the face-on projection (cyan line) is given by the long segment in the lower left-hand corner of the plot. Notice how this segment is about twice larger than the corresponding $\log r_e$ scatter of the FP, given by the short segment at lower left.

of M/L along the ETG sequence, parametrized in terms of galaxy mass, we have to project equation (12), i.e. the FP itself, into the M/L–M plane. To this effect, we can take advantage of a specific projection of the FP, such as the FJ relation, i.e. the fact that luminosity is proportional to σ_0. In this approach, the FJ relation is not providing any extra information with respect to the FP itself, but is used as an empirical tool to project equation (12) into an M/L versus M power law.[5] Using equation (5) to replace σ_0 with L in equation (12), for a given waveband X, we obtain

$$M/L \propto M^{\gamma_x}, \tag{15}$$

[5] A different approach would be that of measuring directly dynamical mass from the data, by means of the virial theorem. This approach (see e.g. JFK96) relies on a given galaxy model to translate σ_0 and r_e into M, and hence implies several assumptions about, for instance, the dark matter component of ETGs. This analysis is currently under way for the SPIDER sample, and will be presented in a forthcoming contribution. For the present study, we adopt a model-independent approach, using only the information provided by the FP.

where

$$\gamma_x = \frac{(\beta_x + \alpha_x\,\lambda)}{(1 + \alpha_x\,\lambda)}, \tag{16}$$

and $\lambda = 0.198 \pm 0.007$ is the average slope of the FJ relation (Section 6). We point out that using the values of λ we have measured for each waveband (see Table 5) rather than the average λ value would not change at all the results presented here. The values of γ, derived with the above procedure, are reported in Table 9 (column 2) for each waveband. The γ has a positive value in all wavebands, and tends to slightly decrease, by 20 ± 5 per cent, from g to K. This variation can be interpreted as a change of stellar population properties along the sequence of ETGs. To this effect, following the same approach of LBM08, we assume that also the stellar mass-to-light ratio of ETGs, M_*/L, is a power law of M:

$$M_*/L \propto M^{\gamma_x^*}. \tag{17}$$

Equation (12) can then be written as

$$M/L \propto M^{\gamma' + \gamma_x^*}, \tag{18}$$

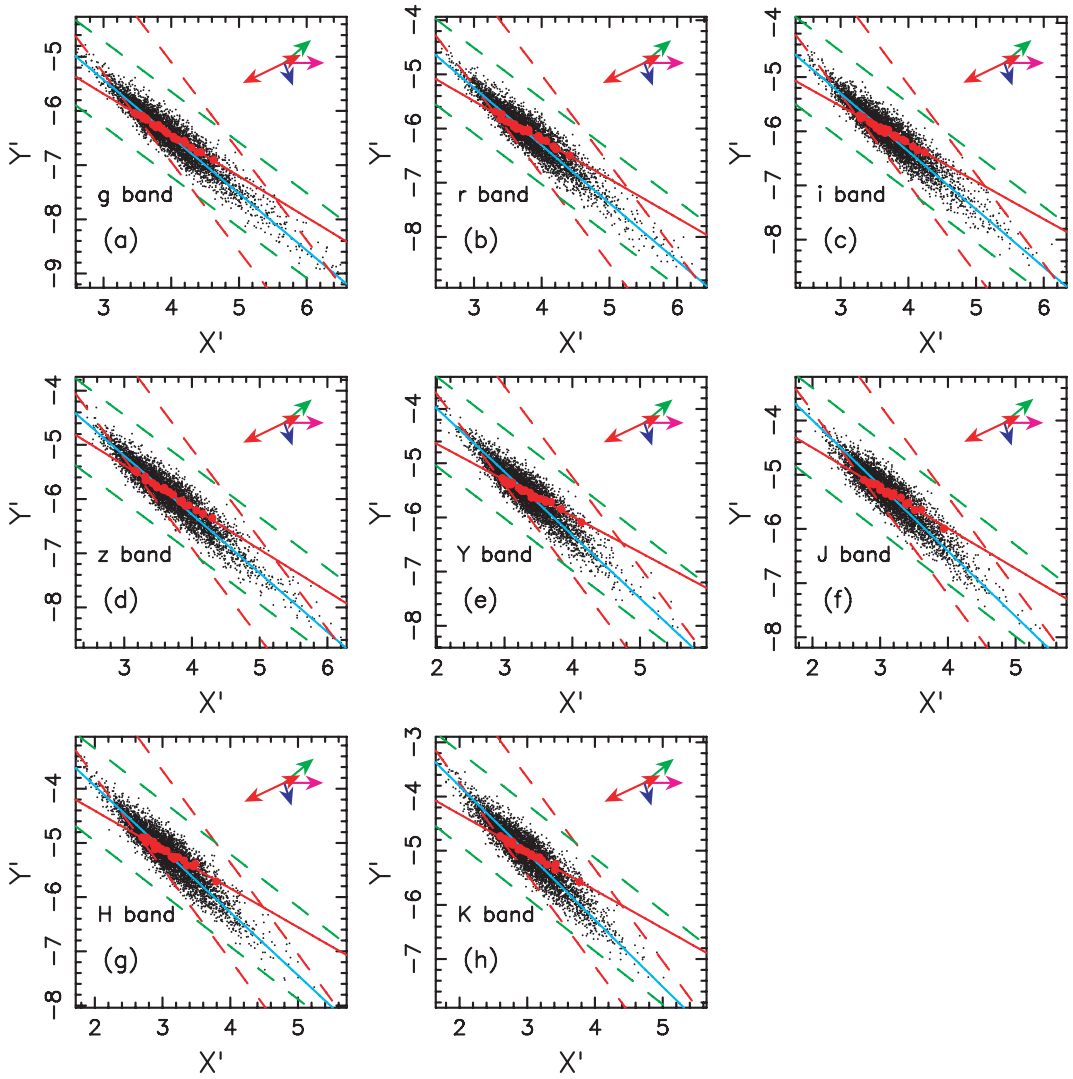

Figure 18. The same as Fig. 17 for the *grizYJHK* wavebands, from left to right, and top to bottom. For better displaying the plots, the internal labels of Fig. 17 are not shown. Panel (b) is the same as Fig. 17 and is repeated to allow a direct comparison with the other panels (wavebands). Notice that for a more direct comparison of the face-on projection in different wavebands, the lengths of the x- and y-axes are the same in all panels.

Table 8. Slopes of the face-on projection of the FP, A' and A'_L, and *predicted* slopes of the FJ and KR, λ'_1 and p'_2.

Band	A' (fit)	A'_L	p'_2	λ'_1
g	-1.05 ± 0.01	-0.77 ± 0.03	3.48 ± 0.02	0.11 ± 0.01
r	-1.08 ± 0.01	-0.72 ± 0.03	3.56 ± 0.03	0.14 ± 0.01
i	-1.07 ± 0.01	-0.69 ± 0.03	3.51 ± 0.03	0.15 ± 0.01
z	-1.09 ± 0.01	-0.78 ± 0.04	3.54 ± 0.03	0.10 ± 0.02
Y	-1.14 ± 0.02	-0.67 ± 0.04	3.64 ± 0.05	0.16 ± 0.02
J	-1.18 ± 0.02	-0.68 ± 0.03	3.66 ± 0.06	0.14 ± 0.02
H	-1.17 ± 0.02	-0.73 ± 0.04	3.67 ± 0.06	0.13 ± 0.01
K	-1.24 ± 0.01	-0.70 ± 0.04	3.83 ± 0.04	0.14 ± 0.01

where $\gamma' = \gamma_x - \gamma^*_x$ defines how the ratio of stellar to total mass changes along the mass sequence of ETGs, $M_*/M \propto M^{-\gamma'}$ and thus it is assumed to be independent of waveband. Introducing the parameter $f = \gamma^*_K/\gamma_K$, which defines the fraction of the K-band slope of the M/L versus M relation due to stellar population effects, we obtain the following system of equations:

$$\left(\frac{1-f}{f}\right)\gamma^\star_K + \gamma^\star_x = \gamma_x. \tag{19}$$

We note that f can vary between 0 and 1. For $f = 0$, the K-band tilt is independent of stellar populations ($\gamma^*_K = 0$), while for $f = 1$ the tilt is entirely explained by stellar population effects ($\gamma^*_K = \gamma_K$ and $\gamma' = 0$). The quantities γ^*_x depend on how stellar population properties change along the mass sequence of ETGs. Considering only the age, t, and the metallicity, Z, one can write

$$\gamma^*_x = \frac{\delta(\log M_*/L)}{\delta(\log M)} = c_{t_x}\frac{\delta(\log t)}{\delta(\log M)} + c_{Z_x}\frac{\delta(\log Z)}{\delta(\log M)}, \tag{20}$$

where the quantities $\delta(\log t)$ and $\delta(\log Z)$ are the logarithmic differences of age and metallicity between more and less massive galaxies (per decade in mass), while $c_{t_x} = (\partial \log M_*/L_x)/(\partial \log t)$ and $c_{Z_x} = (\partial \log M_*/L_x)/(\partial \log Z)$ are the partial logarithmic derivatives of M_*/L (in the waveband x) with respect to t and Z. Deriving the coefficients γ_x from the slope's values of the FP in the different wavebands (equations 13, 14 and 16), and inserting the expression of γ^*_x from equation (20) into equation (19), we obtain a system of

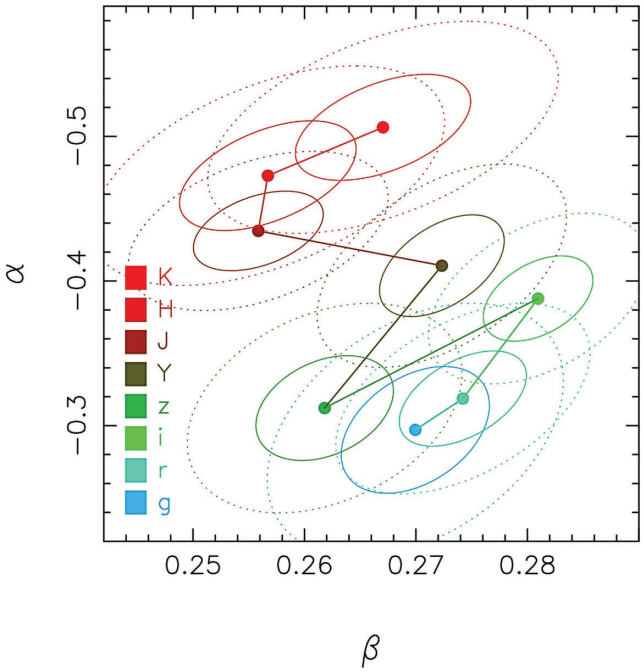

Figure 19. Slopes, α and β, of the power law of M/L as a function of σ_0 and M in the *grizYJHK* wavebands. Solid and dotted ellipses denote 1σ and 2σ confidence contours, respectively, as implied by the uncertainties on FP coefficients (see Table 6).

Table 9. Slopes of the M/L versus mass relation, obtained by projecting the FP through the FJ relation (column 2), by using STARLIGHT (rather than SDSS) σ_0s (column 3) and fitting the γ to the FP coefficients rather than using the FJ relation (column 4).

Waveband	γ		
	SDSS σ_0s	STARLIGHT σ_0s	α–β fit
(1)	(2)	(3)	(4)
g	0.224 ± 0.008	0.251 ± 0.009	0.249 ± 0.008
r	0.225 ± 0.006	0.253 ± 0.007	0.248 ± 0.007
i	0.221 ± 0.006	0.247 ± 0.006	0.254 ± 0.007
z	0.213 ± 0.008	0.236 ± 0.006	0.233 ± 0.007
Y	0.208 ± 0.007	0.230 ± 0.007	0.227 ± 0.007
J	0.186 ± 0.007	0.202 ± 0.008	0.215 ± 0.008
H	0.180 ± 0.009	0.221 ± 0.007	0.208 ± 0.007
K	0.186 ± 0.009	0.218 ± 0.007	0.214 ± 0.008

eight equations, one for each of the *grizYJHK* wavebands, in the three unknowns $\delta(\log t)$, $\delta(\log Z)$ and f. We solved this system by minimizing the sum of relative residuals:

$$\chi^2 = \sum_x \left[\frac{(1-f)/f\,\gamma_K^\star + \gamma_x^\star - \gamma_x}{\gamma_x} \right]^2 . \quad (21)$$

We estimated the quantities $c_{t,x}$ and $c_{Z,x}$ using simple stellar population (SSP) models from different sources: Bruzual & Charlot (2003) (BC03), Maraston (2005) (M05) and Charlot & Bruzual (in preparation) (CB10). These models are based on different synthesis techniques and have different IMFs. The M05 model uses the fuel consumption approach instead of the isochronal synthesis of BC03 and CB10. The CB10 code implements a new AGB phase treatment (Marigo & Girardi 2007). The IMFs are Scalo (BC03), Chabrier (M05) and Salpeter (CB10). Moreover, we also used a composite stellar population model from BC03 having exponential star formation rate (SFR) with e-folding time of $\tau = 1$ Gyr (hereafter BC03$_{\tau\,=1}$). The models are folded with the *grizYJHK* throughput curves, and the M/L values computed for different values of t and Z. In order to evaluate the impact of changing t and Z, we considered three cases, with (i) an age of 9 Gyr and solar metallicity, (ii) an older age of 12 Gyr and solar metallicity and (iii) an age of 12 Gyr and supersolar metallicity ($Z = 1.5\,Z_\odot$). The minimization was performed 2000 times for each kind of model, and for each combination of t and Z values, shifting each time the FP coefficients according to the corresponding (correlated) uncertainties. For each iteration, we found that all the eight equations were solved with an accuracy better than 10 per cent.

Table 10. Age and metallicity differences per decade of galaxy mass.

MODEL	t (Gyr)	$Z/Z_\odot$	$\delta(\log t)$	$\delta(\log Z)$
BC03	12	1	0.013 ± 0.021	0.104 ± 0.026
BC03	9	1	0.013 ± 0.017	0.105 ± 0.025
BC03	12	1.5	0.004 ± 0.001	0.106 ± 0.019
CB10	12	1	0.003 ± 0.021	0.121 ± 0.022
CB10	9	1	0.005 ± 0.025	0.121 ± 0.026
CB10	12	1.5	-0.019 ± 0.004	0.150 ± 0.027
M05	12	1	0.008 ± 0.018	0.112 ± 0.025
M05	9	1	0.012 ± 0.023	0.108 ± 0.022
M05	12	1.5	0.005 ± 0.001	0.094 ± 0.017
BC03$_{\tau\,=1}$	12	1	0.011 ± 0.012	0.107 ± 0.023
BC03$_{\tau\,=1}$	9	1	0.012 ± 0.014	0.107 ± 0.025
BC03$_{\tau\,=1}$	12	1.5	0.006 ± 0.001	0.100 ± 0.018

Fig. 20 plots $\delta(\log t)$ versus $\delta(\log Z)$, as well as the distribution of f values obtained in each case for all the 2000 iterations. For almost all solutions, the f is very close to zero, implying that the tilt of the NIR FP is not due to a variation of stellar population properties of ETGs with mass. For instance, in the case $t = 9$ Gyr and solar metallicity, the percentages of solutions with $f < 0.05$ amounts to 94, 82, 95 and 94 per cent for the BC03, CB10, M05 and BC03$_{\tau\,=1}$ models, respectively. Considering only the solutions with $f < 0.05$, we estimated the mean value of $\delta(\log t)$ and $\delta(\log Z)$. The mean values, and the corresponding uncertainties, are reported in Table 10. The uncertainties were estimated by the standard deviation of the $\delta(\log t)$ and $\delta(\log Z)$ values obtained for a given model and for a given combination of t and Z. The mean values do not depend significantly on either the model or the adopted values of t and Z. On average, $\delta(\log t)$ is very close to zero, while the $\delta(\log Z)$ mean value amounts to $\sim$0.1 dex. This implies that ETGs have synchronous luminosity-weighted ages, with an age variation smaller than a few per cent per decade in mass, while the metallicity variation per mass decade amounts to $\sim$23 per cent. These results remain unchanged when using STARLIGHT rather than SDSS velocity dispersions. Inserting the values of FP coefficients and FJ slope as estimated by STARLIGHT (rather than SDSS) σ_0s in equation (16), the values of the γs increase on average by $\sim$12 per cent, as shown by comparing the values in column 3 (STARLIGHT) and column 2 (SDSS) of Table 9. For instance, the value of γ_g changes from 0.224 (SDSS) to 0.251 (STARLIGHT), while in K band the γ varies from 0.186 (SDSS) to 0.218 (STARLIGHT). Applying the procedure described above to estimate f, $\delta(\log t)$ and $\delta(\log Z)$, we find that, for BC03 SSP models with an age of 9 Gyr and solar metallicity, the corresponding distribution of f values is still strongly peaked around zero, while the mean values of $\delta(\log t)$ and $\delta(\log Z)$ amount to $\sim$0.008 and $\sim$0.100, respectively, fully consistent with what obtained from SDSS σ_0s [$\delta(\log t) \sim 0.013$ and $\delta(\log Z) \sim 0.105$, see Table 10]. As a further test, we estimated the γs by not using the FJ relation. Combining

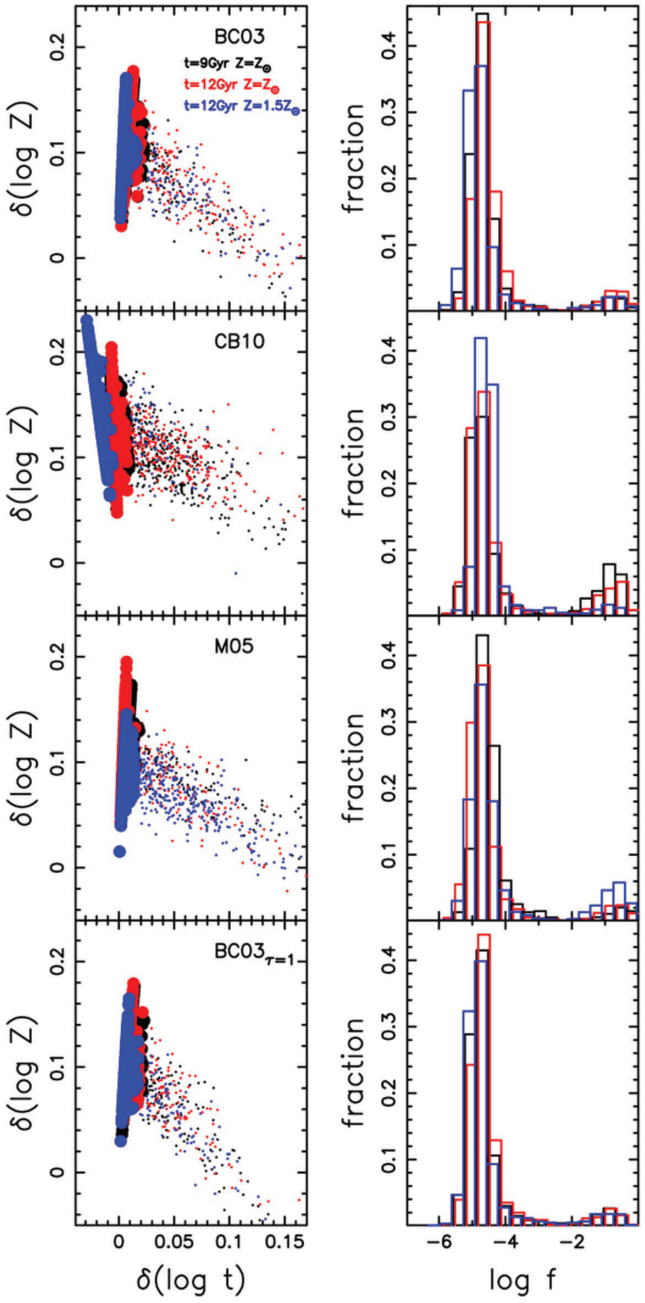

Figure 20. Best-fitting values of $\delta(\log t)$, $\delta(\log Z)$ and f values. The left-hand panels plot $\delta(\log t)$ versus $\delta(\log Z)$ for the BC03, CB10, M05 and BC03$_{\tau=1}$ SSP models (from top to bottom). Different colours denote the different combinations of t and Z as shown in the upper right-hand corner of the top panel. For a given panel and colour, the different points correspond to the solutions obtained in the 2000 minimization iterations. The solutions corresponding to $f < 0.1$ are plotted with larger symbols. The right-hand panels plot the corresponding distributions of f values. To make the plot more clear, small shifts (of ± 0.05) have been applied to the histograms with different colours.

equation (17) with the virial theorem, we obtain the equation

$$\log r_{\rm e} \propto 2\frac{1-\gamma_x}{1+\gamma_x}\log\sigma_0 + \frac{0.4}{1+\gamma_x}\langle\mu\rangle_{\rm e}, \tag{22}$$

which reduces to the FP for $a_x = 2(1-\gamma_x)/(1+\gamma_x)$ and $b_x = 0.4/(1+\gamma_x)$. For each waveband, we estimate the γ_x by minimizing the expression

$$\chi^2 = \left(a_x - 2\frac{1-\gamma_x}{1+\gamma_x}\right)^2/(\delta a_x)^2 + \left(b_x - \frac{0.4}{1+\gamma_x}\right)^2/(\delta b_x)^2, \tag{23}$$

where a_x and b_x are the FP coefficients from Table 6, and δa_x and δb_x are the errors on a_x and b_x. The corresponding values of γ_x are reported in Table 9 (column 4). On average, the values of γ_x tend to increase, with respect to those from equation (16), by ∼13 per cent. Even in this case, this variation does not impact at all the above conclusions, i.e. the f is zero, while the mean values of $\delta(\log t)$ and $\delta(\log Z)$ amount to about 0.01 and 0.1 dex, respectively.

10 DISCUSSION

10.1 The fit of the FP in different wavebands

One of the crucial aspects of the present study is the fitting procedure used to obtain the coefficients of the FP and how they are affected by different systematic effects. Different fitting techniques produce different estimates of FP coefficients, and may lead to erroneous results when comparing the FP relations obtained with different samples (LBC00; Saglia et al. 2001; BER03b). To avoid this problem, we adopt the same fitting method for all the ETG subsamples we analyse. Selection effects and correlated errors on effective parameters can be taken into account analytically under the assumption that the FP variables are normally distributed (Saglia et al. 2001). Although BER03b showed that the joint distribution of $\log r_{\rm e}$, $\log\sigma_0$ and galaxy magnitude is relatively well described by a multivariate Gaussian, this might not necessarily be true when effective parameters are derived by the Sersic (2DPHOT) rather than de Vaucouleurs (PHOTO) model. These two pipelines yield significant differences in $\log r_{\rm e}$ and magnitudes (see Paper I). These differences depend on galaxy magnitude, and may be partly due to the sky overestimation problem affecting the SDSS PHOTO parameters. We have adopted a non-parametric approach, first fitting the FP relation and then correcting the slopes for different systematic effects using extensive Monte Carlo simulations. We find that the main source of bias on the FP slopes is the magnitude cut. In agreement with Hyde & Bernardi (2009), we show that for the orthogonal fit this cut leads to underestimating the FP coefficients, with the effect becoming negligible only at faint magnitude limits ($M_r \sim -18.5$, see Fig. 2). The effect is negligible when we use the $\log\sigma_0$ fitting method. As shown by LBC00, minimizing the $\log\sigma_0$ residuals leads to a $\log\sigma_0$ slope of the FP systematically higher than that obtained by other fitting techniques (see also JFK96). We also find that the coefficient a of the FP in the optical (SDSS) wavebands are systematically larger when we use the $\log\sigma_0$ method compared to results obtained with the orthogonal fitting procedure. In r band the difference amounts to ∼6 per cent. On the other hand, the coefficient b turns out to be systematically lower, by ∼5 per cent, for the $\log\sigma_0$ method (see Tables 6 and 7). Another important result we find is that the difference produced by different fitting method depends on waveband (see also LBM08). The FP coefficients do not change with the waveband when using the $\log\sigma_0$ method, while they smoothly vary, by ∼12 per cent, from g through K when using the orthogonal method. This can be explained by the fact that the $\log\sigma_0$ regression minimizes the rms of residuals in the perpendicular direction to the $\log r_{\rm e}$–$\langle\mu\rangle_{\rm e}$ plane, and hence it is less sensitive to differences in the distribution of galaxies in that plane, like those among effective parameters measured in different wavebands. The problem of deriving the best-fitting coefficients of

correlations among astrophysical quantities has been addressed by Isobe et al. (1990). They concluded that, in case one aims to study the underlying functional relation among the variables, regression procedures treating all the variables symmetrically, like the orthogonal method, should be adopted. For this reason, we have analysed the implications of the waveband dependence of the FP adopting the results of the orthogonal regression.

10.2 Variation of $r_{\rm OPT}/r_{\rm NIR}$ with galaxy radius

In the present study, we find that the slope of the KR exhibits a small systematic variation with waveband, steepening by $\sim$10 per cent from g through K. This variation may be explained as the ratio of optical to NIR effective radii decreasing for galaxies with larger $r_{\rm e}$, namely, while smaller size ETGs have, on average, optical radii larger than the NIR ones, the most massive galaxies have $r_{\rm OPT} \sim r_{\rm NIR}$. In the assumption that $r_{\rm OPT}/r_{\rm NIR}$ is a proxy for the internal colour gradient of an ETG, this finding implies that the stellar populations of the most massive ETGs have a more homogeneous spatial distribution inside the galaxies, i.e. flatter radial gradients, than less massive systems. Spolaor et al. (2009) found that the relation between the internal metallicity gradient and mass in early-type systems is bimodal, with a sharp transition at $M_B \sim -19$. This magnitude corresponds approximately to the lower cut applied to the SPIDER sample (Paper I). For $M_B > -19$, ETGs exhibit a tight correlation between the metallicity gradient and either mass, luminosity or $\log \sigma_0$. Brighter galaxies tend to have steeper gradients, as expected by the lower efficiency of feedback processes in less bound (massive) systems (Larson 1974). At higher mass, colour gradients exhibit a larger scatter, with no sharp dependence on galaxy mass. It is currently not clear how the results of Spolaor et al. (2009) can be reconciled with the variation in the ratio of effective radii with radius we find here. In fact, colour gradients are also determined by the change in the profile shape (i.e. the Sersic index), besides radius, with waveband. Moreover, both metallicity and (small) age gradients can combine to produce the observed internal colour gradients of ETGs (see La Barbera & de Carvalho 2009). The trend of $r_{\rm OPT}/r_{\rm NIR}$ with $r_{\rm NIR}$ is consistent with a recent finding by Roche, Bernardi & Hyde (2009), who analysed how the ratio of effective radii measured in g and r (using SDSS) correlate with several galaxy properties, for different families of ETGs (normal E/S0 galaxies and BCGs). Although limited to the optical regime, they find that the mean ratio of radii measured in g and r become flatter for larger galaxies (Fig. 7). The trend of $r_{\rm OPT}/r_{\rm NIR}$ can be explained by the increasing importance of dissipationless mergers in the formation of more massive galaxies with galaxy mass. Indeed, dry mergers are expected to wash out internal differences of stellar population properties in galaxies (White 1980; di Matteo et al. 2009). A major role of dry mergers in the formation of massive ETGs has also been suggested, in a theoretical framework, by Naab, Khochfar & Burkert (2006) and de Lucia et al. (2006, hereafter deL06).

10.3 The FP from *g* through *K*

LBM08 derived the FP relation in the r (SDSS) and K (UKIDSS) wavebands, showing that the FP slopes exhibit only a small variation with waveband, and that this variation is degenerate with respect to (i) the gradients of stellar population properties (i.e. age and metallicity) with galaxy mass, $\delta(\log t)/\delta(\log M)$ and $\delta(\log Z)/\delta(\log M)$, and (ii) the fraction of the FP tilt, f, which is caused by stellar populations. One main result of the present study is that using the *grizYJHK* coefficients of the FP we are able to break this degeneracy. The resulting probability distribution of f is sharply peaked around zero, implying that the tilt of the FP in the NIR is not due to stellar populations. This result is in agreement with that of Trujillo et al. (2004), who found that the slope of the M/L versus luminosity relation in K band can be entirely due to structural non-homology of ETGs (see also Busarello et al. 1997; Graham & Colless 1997). In B band, they found that a minor but still significant fraction (one-quarter) of the tilt is due to stellar populations. The results of Trujillo et al. (2004) contrast those of Bolton et al. (2007), who argued that the tilt is more likely caused by a variation of the dark matter content with mass, with stellar populations playing a minor role, which fully agrees with our finding. Recently, Jun & Im (2008) have derived the FP relation for a sample of 56 ETGs in the visible (V), NIR (K) and mid-infrared (MIR) [*Spitzer* Infrared Array Camera (IRAC)] wavelengths and concluded that the slope a of the FP increases with the waveband. However, the uncertainties (see their table 2) seem to be still too large to conclude if a increases even further in the MIR wavebands.

Spectroscopic studies of stellar population properties in ETGs have found that the (luminosity-weighted) age of ETGs tends to increase along the galaxy sequence, as parametrized in terms of either velocity dispersion or stellar and dynamical mass (e.g. Thomas et al. 2005; Gallazzi et al. 2006). The ages are usually estimated comparing line spectral indices with the expectations from stellar population models. In particular, Gallazzi et al. (2006) found that the slope of the $\log t$ versus $\log M$ relation is 0.115 ± 0.056 (see their table 4). This value is estimated for a sample of ETGs with a dynamical mass $M \gtrsim 10^{10}\,{\rm M}_{\odot}$, with a limiting magnitude comparable to that we adopt here in this work. The value of $\delta(\log t)/\delta(\log M)$ from Gallazzi et al. (2006) is significantly larger than what we obtain here, although still marginally consistent within 2σ (Table 10). Moreover, we have to consider that age and metallicity values from spectroscopic studies always refer to the central galaxy region. Aperture corrections are based on measurements of line spectral indices for small samples of ETGs at $z \sim 0$ and apply only to a relatively small radial range, with $R < R_{\rm e}$ (see Jørgensen 1997). Gallazzi et al. (2006) adopt a different approach and instead of correcting the indices, test how the stellar population parameters vary with redshift, up to $z \sim 0.12$, for galaxies with similar physical properties (e.g. dynamical mass). The main drawback of this approach is that it relies on the assumption that spectral indices and their gradients do not evolve with redshift. Considering the redshift range ($z < 0.12$), large galaxies are still observed only in a radial region of $R \lesssim R_{\rm e}$. The values of $\delta(\log t)/\delta(\log M)$ and $\delta(\log Z)/\delta(\log M)$ we obtain from the FP analysis describe the total stellar population content of ETGs, as the photometric parameters entering the FP are defined in terms of the total galaxy luminosity of the 2D Sersic model. The information encoded in the FP is more similar to that provided by the CM relation, where galaxy colours are usually measured within a larger aperture than that sampled by spectroscopic studies. In fact, in agreement with our findings, Kodama et al. (1998) showed that the small redshift evolution of the CM relation implies that (i) all the (luminous) ETGs are equally old and (ii) more massive galaxies are more metal rich than less massive systems.

In the framework of the Spectrographic Areal Unit for Research on Optical Nebulae (SAURON) project, for a sample of 25 ETGs, Cappellari et al. (2006) found that the variation of the dynamical M/L is well correlated with the Hβ line strength, implying that most of the tilt of the FP (i.e. the deviation of FP coefficients from the virial theorem expectation under the assumption of homology and constant M/L) is indeed due to galaxy age varying with mass. This

result apparently contrasts with findings of Trujillo et al. (2004) and Bolton et al. (2007), and with our results, where both f and $\delta(\log t)/\delta(\log M)$ are consistent with zero. However, as also noticed by LBM08, 68 per cent of the galaxies in the Cappellari et al. (2006) sample are fast rotators and 20 per cent have low velocity dispersion ($\sigma = 60$–$85\,\mathrm{km\,s^{-1}}$). Zaritsky, Gonzalez & Zabludoff (2006) and D'Onofrio et al. (2008) have found that the FP of spheroidal systems depends on the covered range in mass and velocity dispersion (see also Graham & Guzmán 2008 and references therein), with the tilt becoming larger (smaller a) for galaxies in the low σ_0 regime. Jeong et al. (2009) derived the near-ultraviolet (NUV) and far-ultraviolet (FUV) FP of 34 ETGs from the SAURON sample. They showed that the tilt is significantly affected by residual star formation in ETGs, mostly found at low σ_0 ($\lesssim 100\,\mathrm{km\,s^{-1}}$). Hence, the above-mentioned disagreement with the findings of Cappellari et al. (2006) might be explained by the different range of velocity dispersion and different selection criteria of both samples. It is important to remember, as we have shown in Section 7.3, that different subsamples of ETGs do not share the same FP relations. When binning the SPIDER sample according to Sersic index and axial ratio, we find that the tilt of the FP becomes larger (i.e. the slopes of the FP decrease) by a small but detectable amount for galaxies with higher n and larger b/a, with the effect being mainly due to a difference in the b coefficient of the FP. The result for n is consistent with D'Onofrio et al. (2008), who found that in the optical regime the b coefficient decreases significantly as the Sersic index increases, while a is constant. However, one should notice that D'Onofrio et al. (2008) did not account for the fact that galaxies in different bins of n have different distributions in the space of the FP variables, and, as we show in Section 7.3, this might prevent a proper comparison of FP coefficients. The fact that the variation of the FP tilt among galaxies with different n and b/a is similar from g through K suggests that it is more related to differences of galaxy properties (structural and dynamical), rather than to differences in the galaxy stellar population content. Kelson et al. (2000) derived the FP of 56 ellipticals, lenticulars and early-type spirals in the cluster environment at redshift $z \sim 0.3$. In agreement with JFK96, they found that the FPs of Es and S0s have consistent slopes. They also found that the FP of early-type spirals has a larger tilt (smaller a) with respect to that of ETGs, likely due to a variation of the luminosity-weighted age with galaxy mass. This result might explain what we find when binning the SPIDER ETGs according to their optical–NIR colours and the discy/boxy parameter a_4. Galaxies with bluer colours and more pronounced disc-like isophotes tend to have a more tilted FP (mainly because of a smaller b), with this effect smoothly disappearing from g through K.

10.4 Comparison to semi-analytical models of galaxy formation

Explaining the stellar population properties of ETGs is a lingering problem for theories of galaxy formation and evolution. In the hierarchical scheme of galaxy formation, larger systems assemble their mass at later times. Hence, if star formation closely follows the mass assembling, one would naively expect more massive galaxies to have younger stellar populations, in evident disagreement with (i) the red colours and old stellar populations characterizing the massive ETGs, and (ii) the observed bimodality of galaxies in the CM diagram (Strateva et al. 2001). As shown by Kauffmann (1996), SAMs of galaxy formation in the cold dark matter (CDM) framework can account for point (i) because more massive systems are indeed those forming stars at higher redshift. For massive galaxies, the galaxy bimodality is also reproduced, by preventing cooling flows in the centre of dark matter haloes. This is achieved with some ad hoc recipe, like the feedback from active galactic nuclei (AGN; Croton et al. 2006). As a result, both the luminosity-weighted age and metallicity of ETGs increase from lower to higher mass systems (see fig. 6 of deL06). Since the *grizYJHK* FP sets strong constraints on the variations of age and metallicity with galaxy mass, the natural question is if the amount of such variations can be accommodated in the framework of current models of galaxy formation. Fig. 21 compares the logarithmic variation of age and metallicity per decade in stellar mass, $\delta(\log t)/\delta(\log M_\star)$ and $\delta(\log Z)/\delta(\log M_\star)$, that we infer from the FP[6] (Section 9) and the expectation from SAMs. The plot shows the variation of the mean luminosity-weighted age and stellar metallicities as a function of galaxy stellar mass, $M_\star$, of model elliptical galaxies for the SAM of deL06 (black circles), and that of Wang et al. (2008), where the latter model has been updated according to the 3-yr *Wilkinson Microwave Anisotropy Probe* (*WMAP*3) cosmology. Interestingly, we see that current SAMs are actually able to match the results obtained from the analysis of the FP from g through K. Massive ETGs ($>M_\star \sim 2 \times 10^{10}$) have essentially coeval stellar populations, with more massive galaxies being slightly more metal rich, by a difference in metallicity of $\sim$0.1 dex per decade in mass, than less massive systems.

In a forthcoming paper, we will continue the analysis of scaling relations of ETGs, by presenting the dependence of the FP from g through K as a function of the environment where galaxies reside, and discussing the implications for current models of galaxy formation and evolution.

11 SUMMARY

In this contribution, we present a thorough analysis of the FP of ETGs using a homogeneous data set obtained in two wide-sky surveys (SDSS DR7 and UKIDSS-LAS). As far as the FP derivation is concerned, we discuss fitting procedure, bias due to selection effects, bias due to correlated errors on r_e and $\langle\mu\rangle_\mathrm{e}$ and how to obtain meaningful FP coefficients. Below we summarize some of the main findings of this paper.

(i) We examine the KR for all the wavebands available and find a smooth increase in slope from g ($\sim 3.44 \pm 0.04$) to K ($\sim 3.80 \pm 0.02$), while the scatter seems to be independent of the waveband. Although the KR is just a projection of the FP relation, these results serve as a benchmark at the nearby Universe and will be essential for studies of ETGs at high redshift, for which not always large samples exist to probe the FP. In agreement the waveband variation of the KR slope, we find that the ratio of effective radii measured in g to that measured in K, $(r_{\mathrm{e},g}/r_{\mathrm{e},K})$, decreases as $r_{\mathrm{e},K}$ increases.

(ii) We measure the waveband dependence of the FP with unprecedented accuracy. The trends of the FP coefficients, a and b (see equation 1), with waveband are all very consistent regardless of the sample used (magnitude- or colour selected). When using the $\log\sigma_0$ fit, we find that a is consistent, within 2σ, from r to K and for g band a differs significantly by $\sim 3\sigma$, while b is all very consistent. Using the orthogonal fit, however, a significantly varies by 12 per cent from g through K and b does not change at all.

[6] The quantities $\delta(\log t)/\delta(\log M_\star)$ and $\delta(\log Z)/\delta(\log M_\star)$ are computed from the values of $\delta(\log t)/\delta(\log M)$ and $\delta(\log Z)/\delta(\log M)$ reported in Table 10, and the relation $\delta(\log M) = \delta(\log M_\star)/(1 - \gamma_K)$, that holds for $f = 0$ (see Section 9).

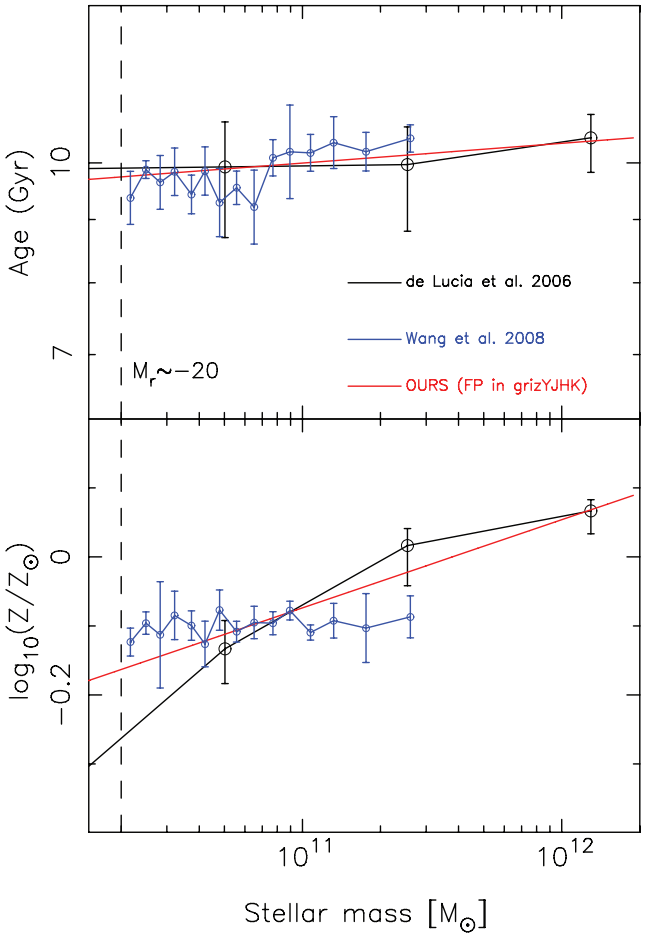

Figure 21. Comparison of the variation of age (upper panel) and metallicity (lower panel) with stellar mass from the *grizYJHK* FP and the predictions of semi-analytical models (SAMs) of galaxy formation. Black circles and error bars are the same as in fig. 6 of deL06, and represent median values of luminosity-weighted age and stellar metallicities of model elliptical galaxies. Black error bars link the upper and lower quartiles of the age and metallicity distribution in a given bin of stellar mass. The magnitude limit of the SPIDER sample corresponds to a stellar mass limit of $\sim 2 \times 10^{10}\,M_{\odot}$, marked in the plot by the vertical dashed line. The blue circles are the peak values of the distributions of luminosity-weighted ages and stellar metallicities for model elliptical galaxies from the updated SAM of Wang et al. (2008), where the *WMAP*3 cosmology (rather *WMAP*1 as in deL06) is adopted. The peak values are computed by the bi-weight estimator. Error bars denote 2σ uncertainties on peak values. Model ellipticals are selected as those objects in the SAM with a stellar mass fraction in the bulge larger than 80 per cent, and colour index $g - r > 0.5$ (consistent with the distribution of ETG's colours for the SPIDER sample, see Paper I). Ages refer to redshift $z = 0$, for both models. The red lines are the result of the analysis of Section 9. Their offset is arbitrarily chosen to match the models, while the slope's are obtained from the values of $\delta(\log t)/\delta(\log M)$ and $\delta(\log Z)/\delta(\log M)$ reported in Table 10 for the BC03 model, with $t = 12$ Gyr and $Z/Z_{\odot} = 1$.

(iii) The analysis of the face-on and edge-on projections of the FP indicates, first of all, consistency with the results obtained when examining the FJ and KR. Moreover, the scatter around the edge-on projection is about twice smaller than that of the face-on's, indicating that the FP is more like a band rather than a plane.

(iv) We test the sensitivity of the FP solution to the velocity dispersion measurement used, $\log \sigma_0$ (STARLIGHT) versus $\log \sigma_0$ (SDSS DR6). Although these two measurements agree remarkably well, the value of a is systematically smaller when using the STARLIGHT values of $\log \sigma_0$, while b is insensitive to both measurements. Furthermore, we find that the waveband dependence of the FP is the same regardless of the magnitude range used in the analysis.

(v) The sample analysed is formed by ETGs covering a certain domain in galaxy properties, like axial ratio (b/a), Sersic index (n), $r - K$ colour and a_4. The FP slopes vary significantly for ETGs with different properties in the following way: ETGs with larger n have lower b; a is smaller in the NIR for the $n > 6$ subsample and in the optical both subsamples have similar as; The FP of round galaxies has smaller a (and smaller b) than the FP obtained for lower b/a ETGs – the difference is more evident in the NIR. Furthermore, boxy and bluer ($r - K$) ETGs exhibit an FP with lower b, with this difference disappearing in the NIR wavebands.

(vi) Finally, we show that current SAMs of galaxy formation match the results here obtained from the analysis of the FP tilt from g through K. This analysis implies that the NIR tilt of the FP is not due to stellar populations: massive ETGs have coeval stellar populations, and are more metal rich than less massive systems. This is one of the crucial points of the FP study presented here.

ACKNOWLEDGMENTS

We thank M. Capaccioli for the support provided to this project. We thank R. R. Gal for several suggestions and comments throughout this project. We thank G. de Lucia and J. Wang for helping us in the comparison to SAMs of galaxy formation. We also thank the anonymous referee for comments which helped us to improve the manuscript. We have used data from the fourth data release of the UKIDSS survey, which is described in detail in Warren et al. (2007). The UKIDSS project is defined in Lawrence et al. (2007). UKIDSS uses the UKIRT Wide Field Camera (WFCAM; Casali et al. 2007). The photometric system is described in Hewett et al. (2006), and the calibration is described in Hodgkin et al. (2009). The pipeline processing and science archive are described in Irwin et al. (in preparation) and Hambly et al. (2008). UKIDSS data have been analysed using the Beowulf system at INAF-OAC (Cascone et al. 2002). Funding for the SDSS and SDSS-II has been provided by the Alfred P. Sloan Foundation, the Participating Institutions, the National Science Foundation, the US Department of Energy, the National Aeronautics and Space Administration, the Japanese Monbukagakusho, the Max Planck Society and the Higher Education Funding Council for England. The SDSS Web Site is http://www.sdss.org/. The SDSS is managed by the Astrophysical Research Consortium for the Participating Institutions. The Participating Institutions are the American Museum of Natural History, Astrophysical Institute Potsdam, University of Basel, University of Cambridge, Case Western Reserve University, University of Chicago, Drexel University, Fermilab, the Institute for Advanced Study, the Japan Participation Group, Johns Hopkins University, the Joint Institute for Nuclear Astrophysics, the Kavli Institute for Particle Astrophysics and Cosmology, the Korean Scientist Group, the Chinese Academy of Sciences (LAMOST), Los Alamos National Laboratory, the Max-Planck-Institute for Astronomy (MPIA), the Max-Planck-Institute for Astrophysics (MPA), New Mexico State University, Ohio State University, University of Pittsburgh, University of Portsmouth, Princeton University, the United States Naval Observatory and the University of Washington.

REFERENCES

Abazajian K. N. et al., 2009, ApJS, 182, 543
Adelman-McCarthy J. K. et al., 2008, ApJS, 175, 297
Beers T. C., Flynn K., Gebhardt K., 1990, AJ, 100, 32
Bender R., Burstein D., Faber S. M., 1992, ApJ, 399, 462
Bernardi M., 2007, AJ, 133, 1954
Bernardi M. et al., 2003a, AJ, 125, 1817
Bernardi M. et al., 2003b, AJ, 125, 1849 (BER03b)
Bernardi M. et al., 2003c, AJ, 125, 1866
Bertin G., Ciotti L., Del Principe M., 2002, A&A, 386, 149
Bolton A. S., Burles S., Treu T., Koopmans L. V. E., Moustakas L. A., 2007, ApJ, 665, 105
Bolton A. S., Treu T., Koopmans L. V. E., Gavazzi R., Moustakas L. A., Burles S., Schlegel D. J., Wayth R., 2008, ApJ, 684, 248
Brosche P., 1973, A&A, 23, 268
Bruzual G., Charlot S., 2003, MNRAS, 344, 1000
Busarello G., Capaccioli M., Capozziello S., Longo G., Puddu E., 1997, A&A, 320, 415
Capelato H. V., de Carvalho R. R., Carlberg R. G., 1995, ApJ, 451, 525
Cappellari M. et al., 2006, MNRAS, 366, 1126
Casali M. et al., 2007, A&A, 467, 777
Cascone E., Grado A., Pavlov M., Capasso G., 2002, in Lewis H., ed., Proc. SPIE Vol. 4848, Telescope & Instrumentation Control Software II. SPIE, Bellingham, p. 328
Cid Fernandes R., González Delgado R. M., Storchi-Bergmann T., Martins L. P., Schmitt H., 2005, MNRAS, 356, 270
Ciotti L., Lanzoni B., 1997, A&A, 321, 724
Ciotti L., Lanzoni B., Renzini A., 1996, MNRAS, 282, 1
Croton D. J. et al., 2006, MNRAS, 365, 11
Dantas C. C., Capelato H. V., Ribeiro A. L. B., de Carvalho R. R., 2003, MNRAS, 340, 398
de Lucia G., Springel V., White S. D. M., Croton D. J., Kauffmann G., 2006, MNRAS, 366, 499 (deL06)
di Matteo P., Pipino A., Lehnert M. D., Combes F., Semelin B., 2009, A&A, 499, 427
Djorgovski S. G., Davis M., 1987, ApJ, 313, 59
Djorgovski S. G., de Carvalho R. R., 1990, in Fabbiano G., Gallagher J. S., Renzini A., eds, Proc. 6th Workshop of the Advanced School of Astronomy, Astrophysics and Space Science Library, Vol. 160, Windows on Galaxies. Kluwer, Dordrecht, p. 9
Djorgovski S. G., de Carvalho R. R., Han M. S., 1988, in Proc. ASP 100th Anniversary Symp., The Extragalactic Distance Scale. Astron. Soc. Pac., San Francisco, p. 329
D'Onofrio M. et al., 2008, ApJ, 685, 875
Dressler A., Lynden Bell D., Burstein D., Davies R. L., Faber S. M., Terlevich R., Wegner G., 1987, ApJ, 313, 42
Faber S. M., Dressler A., Davies R. L., Burstein D., Lynden Bell D., 1987, in Nearly Normal Galaxies: From the Planck Time to the Present. Springer-Verlag, New York, p. 175
Forbes D. A., Ponman T. J., 1999, MNRAS, 309, 623
Gallazzi A., Charlot S., Brinchmann J., White S. D. M., 2006, MNRAS, 370, 1106
Gott J. R., III, Rees M. J., 1975, A&A, 45, 365
Graham A., Colless M., 1997, MNRAS, 287, 221
Graham A., Guzmán R., 2008, Astrophys. Space Sci. Library, 319, 723
Guzmán R., Lucey J. R., Bower R. G., 1993, MNRAS, 265, 731 (GLB93)
Hambly N. C. et al., 2008, MNRAS, 384, 637
Hewett P. C., Warren S. J., Leggett S. K., Hodgkin S. T., 2006, MNRAS, 367, 454
Hjorth J., Madsen J., 1995, ApJ, 445, 55
Hodgkin S. T., Irwin M. J., Hewett P. C., Warren S. J., 2009, MNRAS, 394, 675
Hyde J. B., Bernardi M., 2009, MNRAS, 396, 1171
Isobe T., Feigelson E. D., Akritas M. G., Babu G. J., 1990, ApJ, 364, 104
Jeong H. et al., 2009, MNRAS, 398, 2028
Jørgensen I., 1997, MNRAS, 288, 161
Jørgensen I., Franx M., Kjærgaard P., 1995, MNRAS, 276, 1341
Jørgensen I., Franx M., Kjærgaard P., 1996, MNRAS, 280, 167 (JFK96)
Jørgensen I., Franx M., Hjorth J., van Dokkum P. G., 1999, MNRAS, 308, 833
Jun H. D., Im M., 2008, ApJ, 678, 97
Kauffmann G., 1996, MNRAS, 281, 487
Kelson D. D., Illingworth G. D., van Dokkum P. G., Franx M., 2000, ApJ, 531, 137
Kodama T., Arimoto N., Barger A. J., Aragón-Salamanca A., 1998, A&A, 334, 99
La Barbera F., de Carvalho R. R., 2009, ApJ, 699, L76
La Barbera F., Busarello G., Capaccioli M., 2000, A&A, 362, 851 (LBC00)
La Barbera F., Busarello G., Merluzzi P., Massarotti M., Capaccioli M., 2003, ApJ, 595, 127 (LBM03)
La Barbera F., Merluzzi P., Busarello G., Massarotti M., Mercurio A., 2004, A&A, 425, 797
La Barbera F., de Carvalho R. R., Kohl-Moreira J. L., Gal R. R., Soares-Santos M., Capaccioli M., Santos R., Sant'anna N., 2008a, PASP, 120, 681
La Barbera F., Busarello G., Merluzzi P., de la Rosa I. G., Coppola G., Haines C. P., 2008b, ApJ, 689, 913 (LBM08)
Larson R. B., 1974, MNRAS, 166, 585
Lawrence A. et al., 2007, MNRAS, 379, 1599
Maraston C., 2005, MNRAS, 362, 799
Marigo P., Girardi L., 2007, A&A, 469, 239
Matković A., Guzmán R., 2005, MNRAS, 362, 289
Mobasher B., Guzmán R., Aragón-Salamanca A., Zepf S., 1999, MNRAS, 304, 225
Naab T., Khochfar S., Burkert A., 2006, ApJ, 636, 81
Nelan J. E., Smith R. J., Hudson M. J., Wegner G. A., Lucey J. R., Moore S. A. W., Quinney S. J., Suntzeff N. B., 2005, ApJ, 632, 137
Pahre M. A., Djorgovski S. G., de Carvalho R. R., 1998a, AJ, 116, 1591
Pahre M. A., de Carvalho R. R., Djorgovski R. R., 1998b, AJ, 116, 1606
Roche N., Bernardi M., Hyde J., 2009, MNRAS, submitted (arXiv:0911.0044)
Saglia R. P., Colless M., Burstein D., Davies R. L., McMahan R. K., Wegner G., 2001, MNRAS, 324, 389
Scodeggio M., Gavazzi G., Belsole E., Pierini D., Boselli A., 1998, MNRAS, 301, 1001
Spolaor M., Proctor R. N., Forbes D. A., Couch W. J., 2009, ApJ, 691, 138
Strateva I. et al., 2001, AJ, 122, 1861
Thomas D., Maraston C., Bender R., Mendes de Oliveira C., 2005, ApJ, 621, 673
Tortora C., Napolitano N. R., Romanowsky A. J., Capaccioli M., Covone G., 2009, MNRAS, 396, 1132
Trujillo I., Burkert A., Bell E., 2004, ApJ, 600, 39
Wang J., De Lucia G., Kitzbichler M. G., White S. D. M., 2008, MNRAS, 384, 1301
Warren S. J. et al., 2007, MNRAS, 375, 213
White S. D. M., 1980, MNRAS, 191, 1
Zaritsky D., Gonzalez A. H., Zabludoff A. I., 2006, ApJ, 638, 725

APPENDIX A: THE MLSO FIT

We consider two random variables, X and Y, related by the linear model:

$$Y = p_1 + p_2 X, \tag{A1}$$

where p_1 and p_2 are the offset and slope, respectively. We indicate as x and y the outputs of X and Y. Assuming that the y values are normally distributed along the orthogonal direction to the line, the probability of observing a given x and y pair is

$$P(r)\,\mathrm{d}r = \left(2\pi\sigma_{\rm o}^2\right)^{-1/2} \exp\left[-r^2/\left(2\sigma_{\rm o}^2\right)\right]\,\mathrm{d}r, \quad \text{(A2)}$$

where r is the orthogonal residual, $r = (y - p_1 - p_2 x)(1 + p_2^2)^{-1/2}$, and $\sigma_{\rm o}$ is the orthogonal scatter around the relation. In case where a selection cut is applied,

$$y < c_1 + c_2 x, \quad \text{(A3)}$$

with c_1 and c_2 assigned constants, equation (A2) modifies as follows:

$$P(r)\,\mathrm{d}r = K(p_1, p_2, c_1, c_2; x)\,\exp\left[-r^2/\left(2\sigma_{\rm o}^2\right)\right] \times f(y - c_1 - c_2 x)\,\mathrm{d}r, \quad \text{(A4)}$$

where the function f is equal to one when its argument is smaller than zero, and vanishes otherwise. The function $K(p_1, p_2, c_1, c_2; x)$ is obtained by the normalization condition $\int P(r)\,\mathrm{d}r = 1$. If no selection cut is applied ($f = 1$ identically), one obtains $K = (2\pi\sigma_{\rm o}^2)^{-1/2}$, and we recover equation (A2). In general, the K is given by

$$K = \left(2\pi\sigma_{\rm o}^2\right)^{-1/2}\,2\,[1 + \mathrm{erf}(t)]^{-1}\,, \quad \text{(A5)}$$

with $t = [(c_1 - p_1) + (c2 - p_2)x]\,/(\sqrt{2}\sigma_{\rm o}\sqrt{1 + p_2^2})$, and erf denotes the error function. For a given sample of data points, the likelihood, L, can be written as

$$L = \sum \frac{r^2}{2\sigma_{\rm o}^2} - \sum(\ln K), \quad \text{(A6)}$$

where both sums are performed over the entire data set. In the case of the KR, one has $y = \langle\mu\rangle_{\rm e}$ and $x = \log r_{\rm e}$ (Section 5). The magnitude cut can be written as $\langle\mu\rangle_{\rm e} < M_{\rm lim} + 38.56578 + 5\log r_{\rm e}$, where $M_{\rm lim}$ is the magnitude limit of the sample. This expression is identical to equation (A4) provided that $c_1 = M_{\rm lim} + 38.56578$ and $c_2 = 5$. The MLSO coefficients of the KR are then obtained by minimizing the L with respect to p_1, p_2 and $\sigma_{\rm o}$.

APPENDIX B: MATCHING THE MAGNITUDE AND SURFACE BRIGHTNESS DISTRIBUTIONS OF ETG SAMPLES

We consider the case where a set of n galaxy samples, with running indices $i = 1$ to n, are given. In the case of Section 7.3, we have $n = 2$, and the two samples are obtained by splitting the magnitude-complete sample of ETGs according to a given galaxy parameter p. First, we select the sample with lowest sample size. For such sample, we define the minimum and maximum values of absolute magnitude, $M_{\rm min}$ and $M_{\rm max}$, and the minimum and maximum values of $\langle\mu\rangle_{\rm e}$, $\langle\mu\rangle_{\rm e,min}$ and $\langle\mu\rangle_{\rm e,max}$, respectively. We then construct a grid in the magnitude–$\langle\mu\rangle_{\rm e}$ plane, over the rectangular region from $M_{\rm min}$ to $M_{\rm max}$, and $\langle\mu\rangle_{\rm e,min}$ to $\langle\mu\rangle_{\rm e,max}$. For a given cell k over the grid, we count the number of galaxies of each sample in that cell, $n_{i,k}$. We take the minimum value of $n_{i,k}$, n_k, among all the given samples. For each sample, we then randomly extract n_k galaxies whose magnitude and $\langle\mu\rangle_{\rm e}$ values fall inside the given cell. This step is performed for all the cells in the grid. The procedure provides a subsample of galaxies from each input sample, with all subsamples having the same number of galaxies and the same absolute magnitude and $\langle\mu\rangle_{\rm e}$ distributions. The mean values of $M_{\rm min}$ and $M_{\rm max}$, among the subsamples analysed in Section 7.3, amount to about -24.6 and -20.55, respectively, while the mean values of $\langle\mu\rangle_{\rm e,min}$ and $\langle\mu\rangle_{\rm e,max}$ amount to about 15.2 and 27.2 mag arcsec^{-2}. The step sizes in M and $\langle\mu\rangle_{\rm e}$ are chosen to be 0.2 mag and 0.2 mag arcsec^{-2}, respectively. This makes the number of galaxies in each cell of the grid to be smaller than 40. We verified that either reducing or increasing the bin size in a given direction by a factor of 2 does not change at all the results presented in Section 7.3.

This paper has been typeset from a TEX/LATEX file prepared by the author.